Mediterranean Geoscience Reviews (2021) 3:129–157
https://doi.org/10.1007/s42990-021-00057-6

ORIGINAL PAPER

Cosmogenic data about offset uplifted river terraces and erosion rates: implication regarding the central North Anatolian Fault and the Central Pontides

Aurélia Hubert-Ferrari[1] · Laureen Drab[2] · Jérome Van Der Woerd[3] · Lucilla Benedetti[4] · Jean Van Campenhout[1]

Received: 24 September 2020 / Revised: 30 March 2021 / Accepted: 1 April 2021 / Published online: 30 April 2021

Abstract
River terraces are geomorphological markers recording deformation. Here, we use four strath and fill river terraces along the Kızılırmak River in Turkey to unravel the deformation along the convex arc formed by the central North Anatolian Fault (NAF), a continental transform fault. ^{10}Be, ^{26}Al, ^{36}Cl cosmogenic exposure ages of **T3** and **T2** strath terraces constrain their formation at 83 ± 15 ka and 67 ± 7 ka, respectively. We evidence frost-cracking during humid cold periods that bought younger carbonate cobbles on both terraces. **T1**, a younger fill terrace was probably emplaced during the MIS3 (30–40 ka) aggradational period or during the last glacial–interglacial transition. **T0**, the most recent fill terrace, was incised shortly before the 1668 earthquake based on ^{14}C dating. It records a cumulated 14 ± 2 m offset linked to the 1943 and 1668 earthquakes. **T3** shows a maximum offset of ~ 845 m and constrains a 10 mm/year geological slip rate that is lower than Holocene slip rates. It suggests temporal change in slip rates along the NAF. **T2** and **T3** also evidenced an uplift of 1 mm/year induced by transpressive deformation accommodated close to the NAF. Compared to the 0.28 mm/year obtained to the north, a larger portion of the shortening in the Central Pontides is accommodated close to the driving plate boundary. We also evidenced high cosmogenic-based erosion rates in Pontides during the Holocene, and even higher rates during **T3** planation. Erosion rates were combined with present-day relief to infer a first-order minimal shortening of 12–16 km using simple mass balance principles in the Central Pontides. This long-term shortening is larger than the one induced by the Anatolian rotation suggesting a far field effect of the collision.

Keywords North Anatolian Fault · Transpressive deformation · Cosmogenic dating · Denudation rates · Slip rates · Forst-cracking

1 Introduction

For a transform plate boundary, the plate relative motion is defined by the rotation around a given Eularian pole, and a pure transform fault follows a small circle around this pole. When the transform fault geometry differs from a small circle, it results into extensional or compressional deformation. Over the life span of the fault, large subsiding sedimentary basins and mountain ranges are, thus, formed. An example of the later is the convex bend of the North Anatolian Fault (NAF) in its central part.

The NAF in the eastern Mediterranean area is a ~ 1500 km long right-lateral transform fault and its geometry is similar to a small circle around an Eulerian pole located near the Sinai (Reilinger et al. 2006). The NAF accommodates the extrusion of the Anatolian microplate westward toward the Aegean subduction zone (Fig. 1). Here, we focus on its central northward convex arc where the fault curvature is narrower than the ideal small circle for a smooth rotation of the Anatolian microplate (Fig. 1). Right-lateral deformation is attested at different scale along this central segment of the NAF (e.g., Hubert-Ferrari et al. 2002) that last ruptured last

✉ Aurélia Hubert-Ferrari
aurelia.ferrari@uliege.be

[1] Department of Geography, Sart Tilman, Quartier Village 4, clos Mercator 3, 4000 Liège 1, Belgium

[2] Beicip Franlab, 92502 Rueil-Malmaison, France

[3] Active Tectonique IPGS-EOST, 5, rue René Descartes, 67084 Strasbourg, France

[4] CEREGE UMR CNRS 6635, Université Aix-Marseille III, Europole Méditerranéen de L'Arbois, BP 80, 13545 Aix en Provence, France

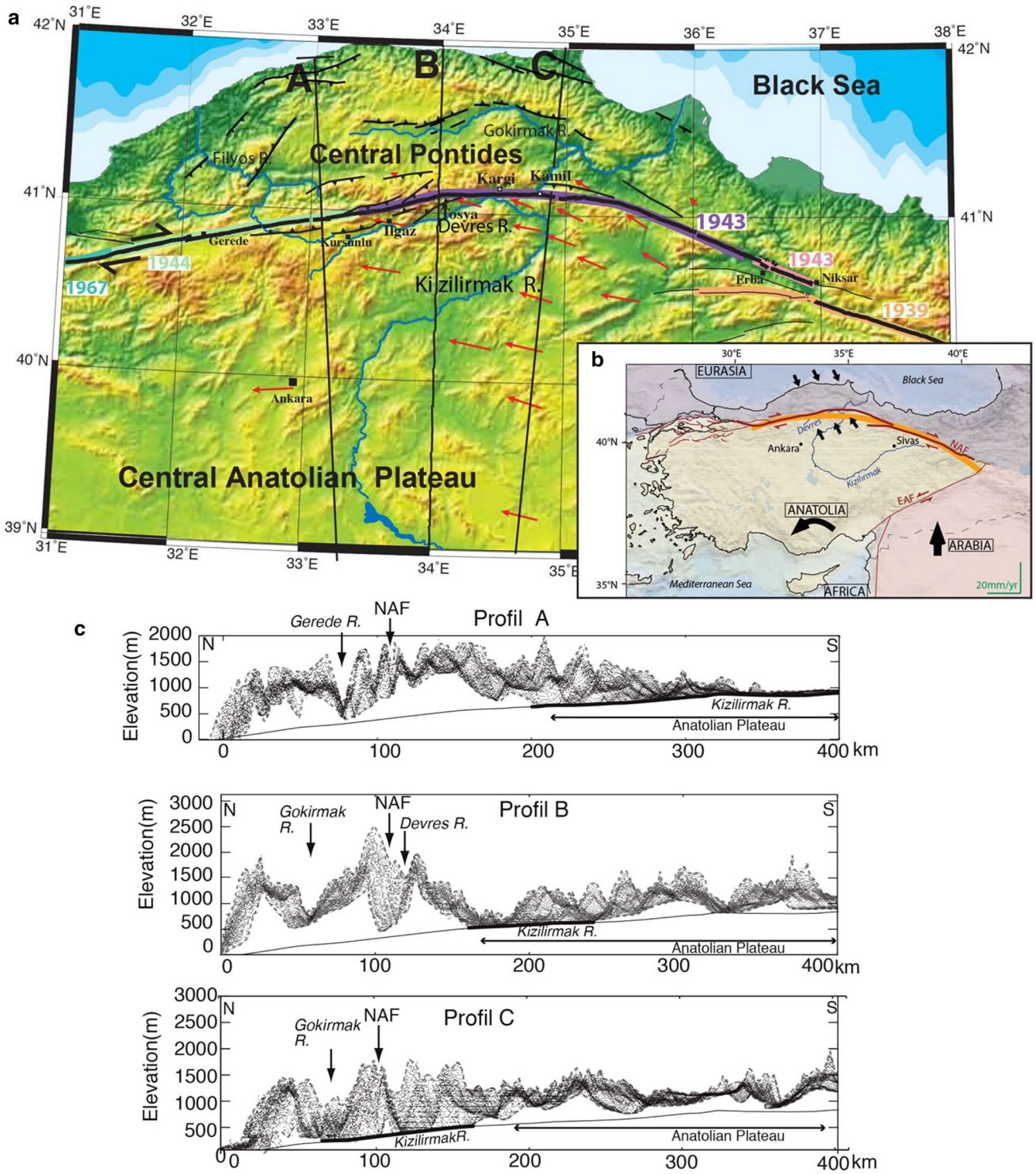

Fig. 1 Geodynamic setting. **a** The central NAF forming a broad convex arc, and secondary thrust faulting in the CP orogenic wedge; river network is indicated in blue; location of A, B, C profiles is displayed below in (**c**); red arrow is GPS vectors from Yavaşoğlu et al. (2011); strike-slip faulting from Hubert-Ferrari et al. (2002) and thrust faulting from Yıldırım et al. (2011); NAF ruptures from Barka (1996). **b** Inset with the Anatolian plate bounded to the north by the NAF; thick orange line indicates the geometry of the Eulerian small circle best fitting the NAF geometry in its central and eastern parts, small black arrows evidence the compression resulting from the difference in geometry between the Eulerian circle and the NAF, and large arrows the schematic plate motion. **c** Three swath profiles perpendicular to the NAF evidencing the relief of the CP resulting from shortening. Swath profiles are 50 km wide and display all gridded points of GTOPO30 data contained in the swath

in 1943 (e.g., Barka 1996), but the large-scale fault geometry also generates compressional fault-normal deformation. This deformation is accommodated in a ~ 200 km wide area called the Central Pontides (CP), which also defines the northern edge of the uplifted Central Anatolian Plateau (CAP). Compression in the CP is attested by a wide array of evidences. Geodetic observations show that the Anatolian motion with respect with Eurasia is not parallel to the NAF, implying a significant compressive deformation (Fig. 1) (Kreemer et al. 2003; Reilinger et al. 2006; Allmendinger et al. 2007; Yavaşoğlu et al. 2011). Microseismicity evidences that deformation is accommodated by NE–SW thrust faulting and by transpression along the central NAF (Karasözen et al. 2013). Active uplift in the CP was confirmed by regional morphometry and geomorphic observations made by Yıldırım et al. (2011, 2013a); they proposed a geodynamical model where the CP would be an active orogenic wedge extending from the Central Anatolian Plateau to the Black Sea coast. Deformation would result from a positive flower-structure geometry and be developed over a shallow detachment surface linked to the NAF at depth.

The relationship between the NAF strike-slip motion and shortening within the CP wedge still remains an open question. We focus here on a set of strath and fill terraces mostly in the Kamil Basin that are deformed by the NAF, and on watersheds potentially affected by folding and thrusting along the NAF. We make use of these different geomorphological markers to provide new data about uplift, long- (10–100 ka) and short- (< 10 ka) term horizontal deformation along the NAF. First, we use cosmogenic-based erosion rates to constrain Holocene denudation rates in the CP. Second, cosmogenic dating on two strath terraces allows us to discuss the terrace formation, origin and incision, to infer their uplift and a new long-term geological slip rate along the central NAF. Third, geomorphological mapping, field survey, radiocarbon dating and trenching across recent terraces provide new data about the last two earthquake ruptures. Finally, these geomorphological and cosmogenic data allow us to discuss the terrace formation, origin and incision, to infer a new geological slip rate along the central NAF, to evaluate the uplift gradient in the CP and to obtain a first-order evaluation of cumulated shortening in the CP to be compared with the one deduced from the NAF kinematics.

2 Tectonic geomorphology of the NAF along its central part

2.1 Strike-slip deformation

Strike-slip deformation is mostly localized along a narrow zone as attested by right-lateral offsets at a range of scale (e.g., Hubert-Ferrari et al. 2002), even if shearing also occurs in wider zone (Barka and Hanccok 1984; Barka 1984; Şengör et al. 2005). The Kızılırmak River between the Kargı and the Kamil releasing structures (Barka and Kadinsky-Cade 1988) shows a right-lateral offset of 30 km (e.g., Hubert-Ferrari et al. 2002; Fraser et al. 2010a). At a smaller scale, the offset morphology on both sides of the Kızılırmak River imply a slip rate of $18.6 + 3.5/-3.3$ mm/year (Kozacı et al. 2009), 18 ± 3.5 mm/year (Hubert-Ferrari et al. 2002), 20.5 ± 5.5 mm/year (Kozacı et al. 2007) depending on the studied site [see also review by Zabcı (2019)]. This is close to slip rates ranging from 18.7 ± 1.6 to 21.5 ± 2.1 mm/year derived from local GPS data (Yavaşoğlu et al. 2011; Aktuğ et al. 2015) and to the 21 mm/year (14–29, 95% CI) rate derived from InSAR (Hussain et al. 2016) or ERS data (Peyret et al. 2013). Elastic block-models (e.g., Reilinger et al. 2006) suggest slightly faster rates, the most recent one of Aktuğ et al. (2015) gave a 22.5 ± 0.4 mm/year rate. The slightly lower geological slip rates compared to the geodetic ones have been attributed to slip distributed on secondary structures (Zabcı 2019).

There are only two small geometrical discontinuities along the central NAF (Figs. 1a, 2): the Kargı and Kamil releasing step-overs that the Kızılırmak River exploits to cross the CP. These discontinuities have not been capable of stopping the past historical earthquakes. The 1943 earthquake ruptured the whole central NAF from west to east over 280 km (Barka 1996). The antecedent 1668 earthquake also broke the NAF central bend (Ambraseys and Finkel 1988). Paleoseismic trenching has revealed that strain along this segment is released with a relative temporal uniformity (Fraser et al. 2010a). There are few co-seismic slip measurements about both earthquakes around Kamil. The 1943 co-seismic slip of 1.4 and 2.6 m was measured at two locations near Kamil (Barka 1996), and Fraser et al. (2010a) infer a probable 10 m slip during the 1668 earthquake at the Elmacik trench site east of Kamil.

2.2 Shortening and uplift in Central Pontide orogenic wedge

Distributed shortening occurs uplifting the CP orogenic wedge. It is mostly attributed to the present geodynamics (Yıldırım et al. 2011, 2013a, b). The inferred pseudo-paleotopography of Sunal and Erturaç (2012) indicates no specific topographic rise, but topographic swath profiles show the resulting high topographic bulge centered along the NAF (Fig. 1c). The profiles highlight the following characteristics and changes in topography (Fig. 1c). The lowest altitudinal levels correspond to the Kızılırmak floodplain that extends over 1350 km from the Central Anatolian Plateau to the Black Sea coast. Since ~ 2.5 Ma, the Kızılırmak River has slowly incised the Anatolian Plateau (Doğan 2010, 2011; Çiner et al. 2015), which was initially internally drained; it

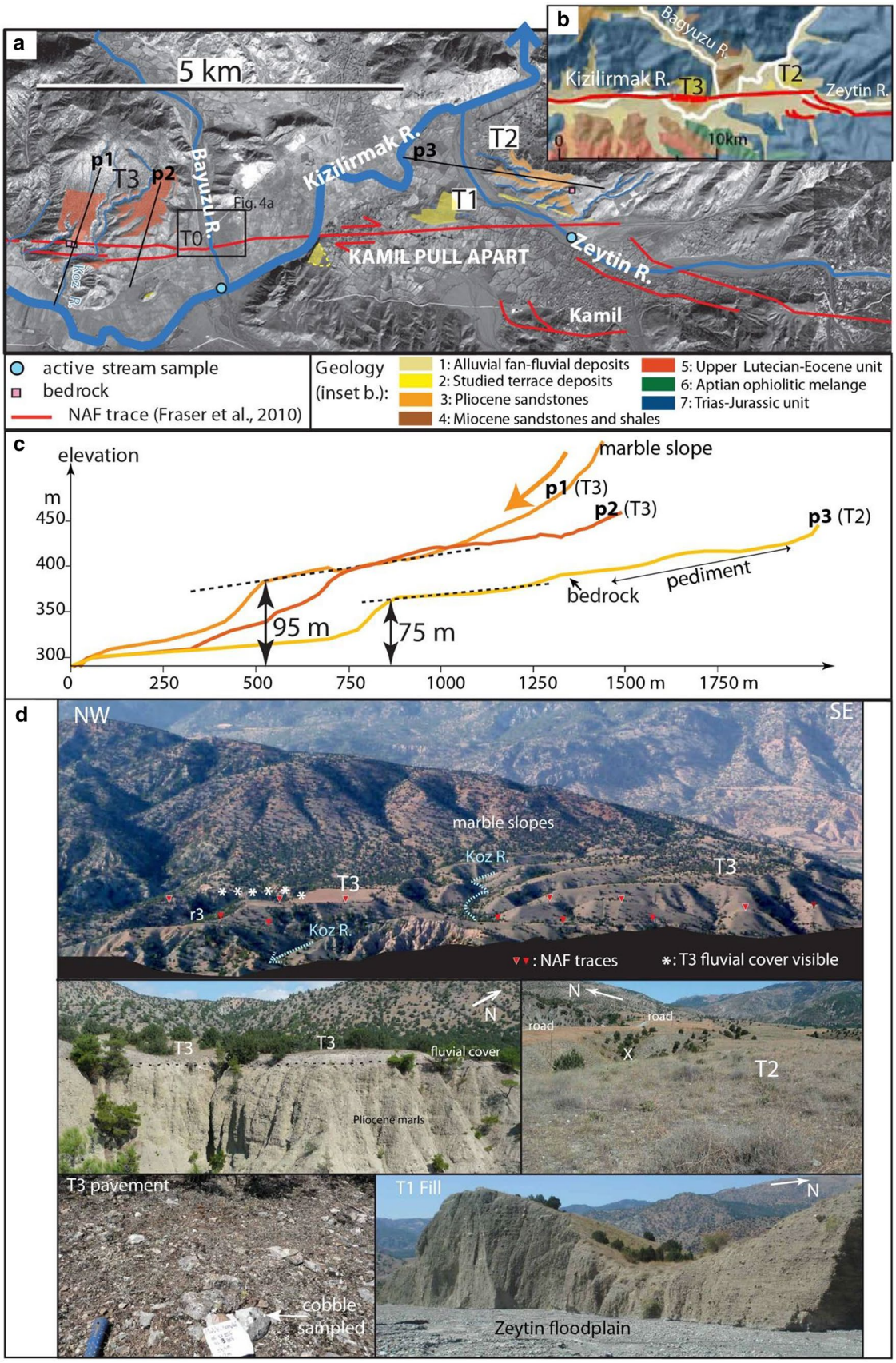
a
5 km
p1
T3
p2
Bayuzu R.
Fig. 4a
T0
Kizilirmak R.
p3
T2
T1
KAMIL PULL APART
Zeytin R.
Kamil
Koz R.
b
Bagyuzu R.
Kizilirmak R.
T3
T2
Zeytin R.
0
10km
active stream sample
bedrock
NAF trace (Fraser et al., 2010)
Geology (inset b.):
1: Alluvial fan-fluvial deposits
2: Studied terrace deposits
3: Pliocene sandstones
4: Miocene sandstones and shales
5: Upper Lutecian-Eocene unit
6: Aptian ophiolitic melange
7: Trias-Jurassic unit
c
elevation
m
450
400
350
300
marble slope
p1 (T3)
p2 (T3)
p3 (T2)
bedrock
pediment
95 m
75 m
0
250
500
750
1000
1250
1500 m
1750 m
d
NW
SE
marble slopes
Koz R.
T3
r3
Koz R.
T3
: NAF traces
*: T3 fluvial cover visible
N
T3
T3
fluvial cover
Pliocene marls
N
road
road
X
T2
T3 pavement
cobble sampled
T1 Fill
N
Zeytin floodplain

◂**Fig. 2** Maps and characteristics of terraces in Kamil Basin. **a** Location with respect to the NAF and the river network on an Ikonos image; frame of Fig. 6a is indicated. **b** Location with respect to geology from Herece and Akay (2003) accordingly unit 5 represents andesitic and basaltic rocks; unit 7, schists–marbles and metabasites. **c** Topographic profiles showing characteristics of T2 and T3 strath terraces standing, respectively, 75 and 95 m above the floodplain; in p1, the connection of T3W with the hillslope is evidenced and in p3, the continuity of T2 with a bedrock outcrop and a pediment. **d** Photographs of T1, T2 and T3. *Top*: view of T3 from the south with the NAF location and the T3 visible alluvial cover indicated. *Middle right*: view of T3 carved in Pliocene marls with a restricted alluvial cover. *Middle left*: T2 and gully erosion in its surface (gully is labeled X) with the road built on it in the background. *Bottom*: view of the T1 20–25 m thick fill terrace on the southern edge of T2 (Fig. 4b)

established its present course across the NAF and its outlet at the Black Sea coast around 2 Ma (Hubert-Ferrari et al. 2002; Şengör et al. 2005; Yıldırım et al. 2011). The Central Anatolian Plateau is easily identified by a topography with a reduced relief (i.e., profile A in Fig. 1c). Just to the north of the Anatolian Plateau, the relief rises in relation with the CP, a Late Cretaceous to early Tertiary mountain range related to the Tethyan closure (Sengör and Yılmaz 1981; Okay et al. 1999; Cavazza et al. 2012; Okay et al. 2020) that sustained different phases of deformation (Ballato et al. 2018). The shortening may have been followed by a post-collisional extensional/transtensional phase (e.g., Çinku et al. 2011; Ottria et al. 2017). More to the north (i.e., ~ 200–100 km south of the Black Sea coast), the CP topography increases and reaches a maximum close to the NAF in the Ilgaz Mountains (i.e., profile B in Fig. 1c).

Different structures accommodated the present shortening. At the location of the Black Sea coast, marine terraces were uplifted at a rate of 0.02–0.26 mm/year (Yıldırım et al. 2013b) and of 0.28 ± 0.07 mm/year (Berndt et al. 2018). More to the south there are two distinct deformational belts: the Sinop and the Ilgaz ranges (Fig. 1a). The Sinop push-up structure is characterized by south-vergent thrusts (Andrieux et al. 1995; Yıldırım et al. 2011, 2013a), and terraces and pediments have been uplifted at a rate of ~ 0.3 mm/year over the past ~ 350 ka (Yıldırım et al. 2013a). The Ilgaz push-up structure is centered along the NAF (Andrieux et al. 1995; Yıldırım et al. 2011, 2013a), and major compressive structures bound the Tosya, Ilgaz and Cerkes sedimentary basins (Barka 1984; Over et al. 1993; Andrieux et al. 1995; Hubert-Ferrari et al. 2002). These structures are supposed to be seismically active, and the block model of Aktuğ et al. (2015) implies 4.5 mm/year shortening rate.

3 Denudation of the Kızılırmak watersheds in the CP Range along the NAF

To evaluate the denudation of the CP Range, we seek to obtain catchment-averaged denudation rates using cosmogenic nuclide concentrations. We focus on the Kızılırmak catchment directly affected by the NAF within the CP orogenic wedge, and sampled 9 river catchments: the Kızılırmak River (present-day and past river beds), three of its main tributaries, the Devrez, the Zeytin and the Bağyüzü Rivers, and five subparallel tributaries of the Devrez River (Fig. 3).

3.1 Cosmogenic-based erosion rates

To obtain ^{10}Be–^{26}Al concentrations, we sample the sandy fraction of 11 active riverbeds that have the following characteristics (Fig. 3). The Kızılırmak River has a 78,180 km^2 watershed that covers a wide variety of geological terrains: sedimentary, magmatic and metamorphic bedrocks from Mesozoic to Neogene. Within the study area, the Kızılırmak River flows along the NAF for ~ 30 km between the Kargı and the Kamil tectonic basins. These basins are at the confluence sites of the Devrez River and the Zeytin/Bağyüzü Rivers, respectively, with the Kızılırmak River. The Bağyüzü catchment is located just north of the Kamil Basin, and the Zeytin catchment is located just to the east; the later main river trunk flows for ~ 13 km close to the NAF. Geological maps (Herece and Akay 2003) show that the catchment lithology is poor in quartz and comprises mostly metamorphic rocks (mostly marbles) from Trias to Jurassic; other geological units (Upper Cenomamian clastic and carbonanates rocks; ophiolites) have restricted extension. The Devrez catchment is located west of the Kargi Basin and can be divided into two parts. To north of the main river trunk, there are first, the Tosya and Ilgaz sedimentary basins and then the Ilgaz Mountain Range; this area is affected by active folding and thrusting (Hubert-Ferrari et al. 2002; Yıldırım et al. 2011). To the south and in its head water, lower ranges with less steep slopes are found (Figs. 1, 3). The northern part of the Devrez catchment lithology comprises formations deposited before the Eocene, mostly similar to ones in the Zeytin catchment, as well as younger continental clastic sediments of the Pontus Formation filling the Tosya and Ilgaz Basins (Barka 1984; Hubert-Ferrari et al. 2002). All sampled tributaries of the Devrez River are located north of this river (Fig. 3). Four of these tributaries extend from the Ilgaz Mountains to the Tosya Basin, and one extends from the Ilgaz Mountains to the Ilgaz Basin. In the upstream part of these steep mountainous catchments, the pre-Eocene lithology outcrops, and downstream the Pontus formation. Samples were taken in active riverbeds along main river trunks before of confluence with larger rivers (Fig. 3).

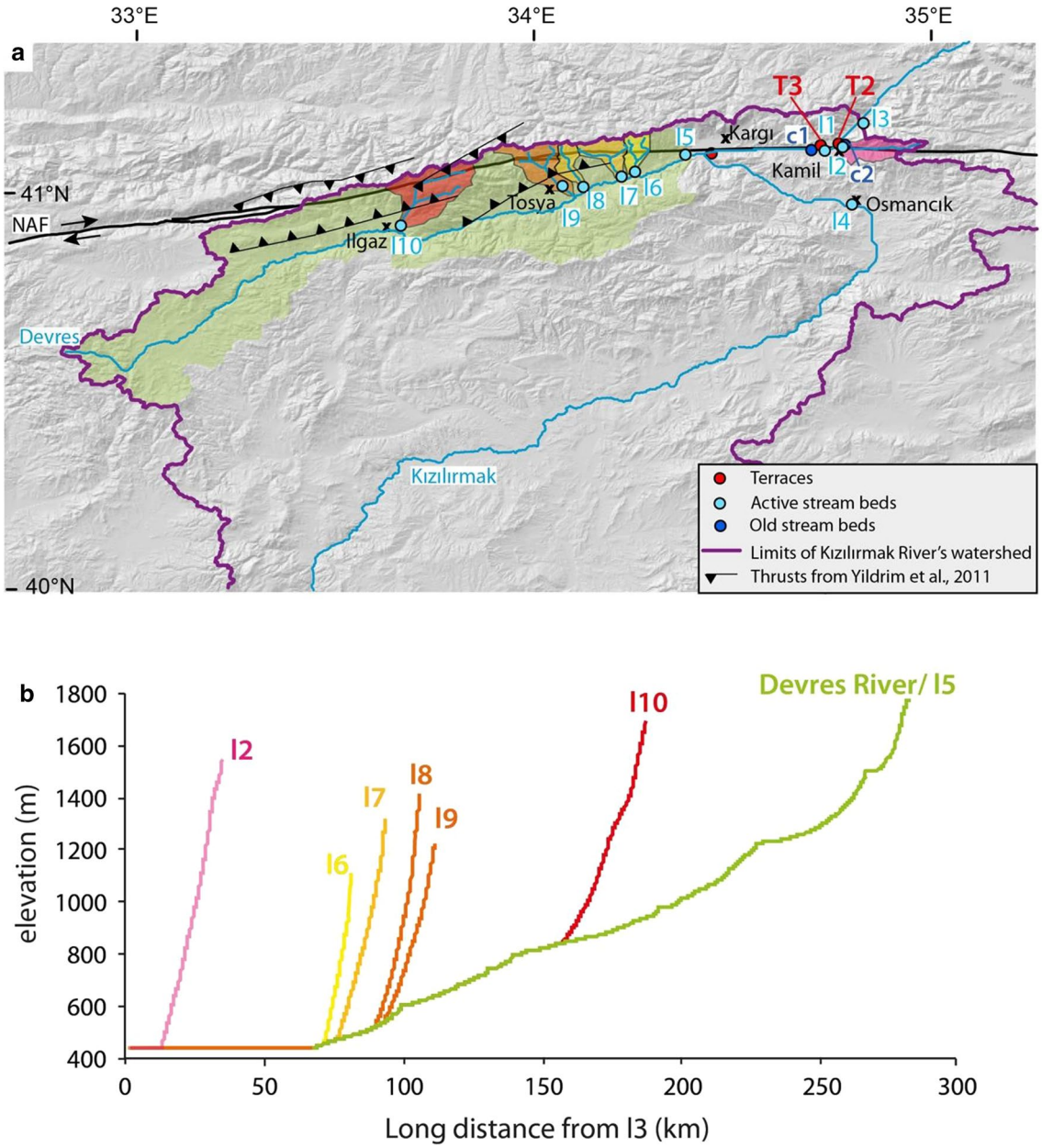

Fig. 3 Studied watersheds for erosion rates. **a** Location of the rivers sampled for cosmogenic-based erosion rates. The studied catchments are outlined with different colors. **b** River profiles of some studied catchments

We also sampled former river beds of the Kızılırmak River at two locations. These sand samples were collected in depth profiles above the **T2** and **T3** strath surfaces in the Kamil Basin (Figs. 3 and S1). In terrace **T3**, there was only one reachable depth section along the southern terrace edge; it was located in a cliff along a rounded terrace edge (Figs. 2, 3). Three samples were collected in sandy layers along this profile (samples T3-sand-1, 2, and 3; Tables 1 and S1; Figure S1); the lowest one is located just above the strath–alluvium contact and was deposited during strath planation. The depth of the three samples was corrected by ~ 40 cm based on the terrace edge shape (see Figure S1). In terrace T2, only one depth section was found at the road cut at its eastern extremity; at that location, the alluvial deposit was covered by a debris flow (Fig. 2). Two sand samples were collected (T2-sand-1 and 2; Tables 1 and S1; Figure S1); the upper one was located in a small paleochannel, and the lower one just above the 60 cm thick basal gravel layer that is likely to be associated with the strath planation.

For all samples, sieving was performed to keep only the 150–250 micron fraction. We used the same preparation technics as for the terrace surface samples (see below) and

Table 1 ^{10}Be-^{26}Al samples: AMS results, Cronus model age (no inheritance, no erosion), and erosion rates (density 2.7 for all samples). Sample locations in Table S1

Samples	Be measurements				Age	Erosion	Al measurements				Age	Erosion
	Quartz	^{9}Be carrier	^{10}Be/^{9}Be	^{10}Be	^{10}Be age	^{10}Be Erosion rate	^{27}Al natural	^{27}Al carrier added	^{26}Al/^{27}Al	^{26}Al	^{26}Al age	^{26}Al Erosion rate
	(g)	(mg)	($\times 10^{-13}$)	(at/g qtz)	(years)	(m/Ma)	(mg)	(mg)	($\times 10^{-13}$)	(at/g qtz)	(years)	(m/Ma)
T3-3	24	0	4,56,414 ± 0,12,978	613,515 ± 21,328	98,976 ± 9493	–	0,86	1,30	15,09,648 ± 0,43,872	3,024,445 ± 185,074	82,243 ± 9101	–
T3-4	1	0	0,2505 ± 0,01,305	413,535 ± 23,083	63,712 ± 6684	–	0,23	2,14	0,54,527 ± 0,05,223	2,840,362 ± 312,111	74,138 ± 10,772	–
T3-5	21	1	2,93,369 ± 0,08,785	459,017 ± 16,528	71,273 ± 6822	–	1,75	0,27	13,09,778 ± 0,40,262	2,745,533 ± 170,244	72,009 ± 7963	–
T2-2	7,55,093	0,24,825	0,93,717 ± 0,03,001	206,164 ± 7782	31,379 ± 2995	–	0,55	1,33	2,31,193 ± 0,11,674	1,279,913 ± 94,484	32,606 ± 3777	–
T2-5	8,87,072	0,24,989	0,69,218 ± 0,03,914	130,471 ± 7825	20,435 ± 2168	–	4,63	0,00	0,66,174 ± 0,06,061	770,359 ± 80,384	20,123 ± 2759	–
T2-10	13,5749	0,25,188	3,50,987 ± 0,10,864	435,756 ± 16,059	69,852 ± 6707	–	47,04	0,00	Not reliable			–
T2-11	20,74,936	0,50,205	3,17,795 ± 0,10,378	514,499 ± 19,701	84,799 ± 8223	–	0,47	1,74	14,18,664 ± 0,40,934	3,372,687 ± 206,052	94,586 ± 10,526	–
T2-12	20,93,114	0,50,572	1,2883 ± 0,03,977	208,273 ± 7660	33,925 ± 3227	–	0,81	0,65	8,55,187 ± 0,25,132	1,329,743 ± 81,577	36,281 ± 3928	–
T2-13	20,54,854	0,50,544	2,21,847 ± 0,06,394	365,127 ± 12,808	57,637 ± 5478	–	0,38	1,44	8,45,114 ± 0,26,303	1,665,464 ± 103,589	43,954 ± 4799	–
L1	25,7809	0,25,042	0,23,857 ± 0,03,463	15,505 ± 2272	–	482 ± 120	45,41	0,00	0,00,883 ± 0,00,883	34,697 ± 34,742	–	Unreliable
L2	1,04,737	0,24,772	0,0333 ± 0,00,563	52,693 ± 8970	–	134 ± 36	0,42	1,36	0,02,287 ± 0,01,144	86,702 ± 43,605	–	604 ± 425
L5	25,0548	0,25,228	0,54,992 ± 0,07,113	37,050 ± 4849	–	201 ± 48	53,39	0,00	0,01,458 ± 0,01,031	69,295 ± 49,123	–	Unreliable
L6	12,22,249	0,25,185	0,08,488 ± 0,01,157	11,702 ± 1612	–	710 ± 170	6,41	0,00	0,01,791 ± 0,01,034	20,939 ± 12,135	–	Unreliable
L7	23,2152	–	–	–	–		56,93	0,00	0,00,949 ± 0,00,949	51,902 ± 51,968	–	Unreliable
L8	17,3141	0,25,162	0,2671 ± 0,01,763	25,972 ± 1791	–	324 ± 67	31,51	0,00	0,04,263 ± 0,01,907	173,033 ± 77,873	–	360 ± 215
L9	20,1526	0,25,043	–	–	–		68,37	0,00	0,02,319 ± 0,0116	175,476 ± 88,183	–	357 ± 250
L10	21,76,207	0,50,149	0,10,887 ± 0,03,148	16,786 ± 4864	–	514 ± 191	46,46	0,00	0,01,785 ± 0,0103	84,977 ± 49,248	–	751 ± 672
L3	31,4521	–	–	–	–	–	63,33	0,00	0,03,234 ± 0,01,451	145,228 ± 65,587	–	380 ± 220
T3–sand1	20,8317	0,25,132	0,9582 ± 0,03,061	77,350 ± 2915			19,02	0,00	0,17,923 ± 0,0317	365,033 ± 67,103	–	
T3–sand2	35,03,711	0,50,266	–	–			50,13	0,00	0,16,636 ± 0,03,329	530,841 ± 109,491	–	
T3–sand3	39,4853	0,49,031	–	–			43,95	0,00	0,10,279 ± 0,03,019	255,196 ± 76,036	–	
T2–sand1	14,0597	0,25,104	0,4378 ± 0,09,923	52,304 ± 11,901							–	

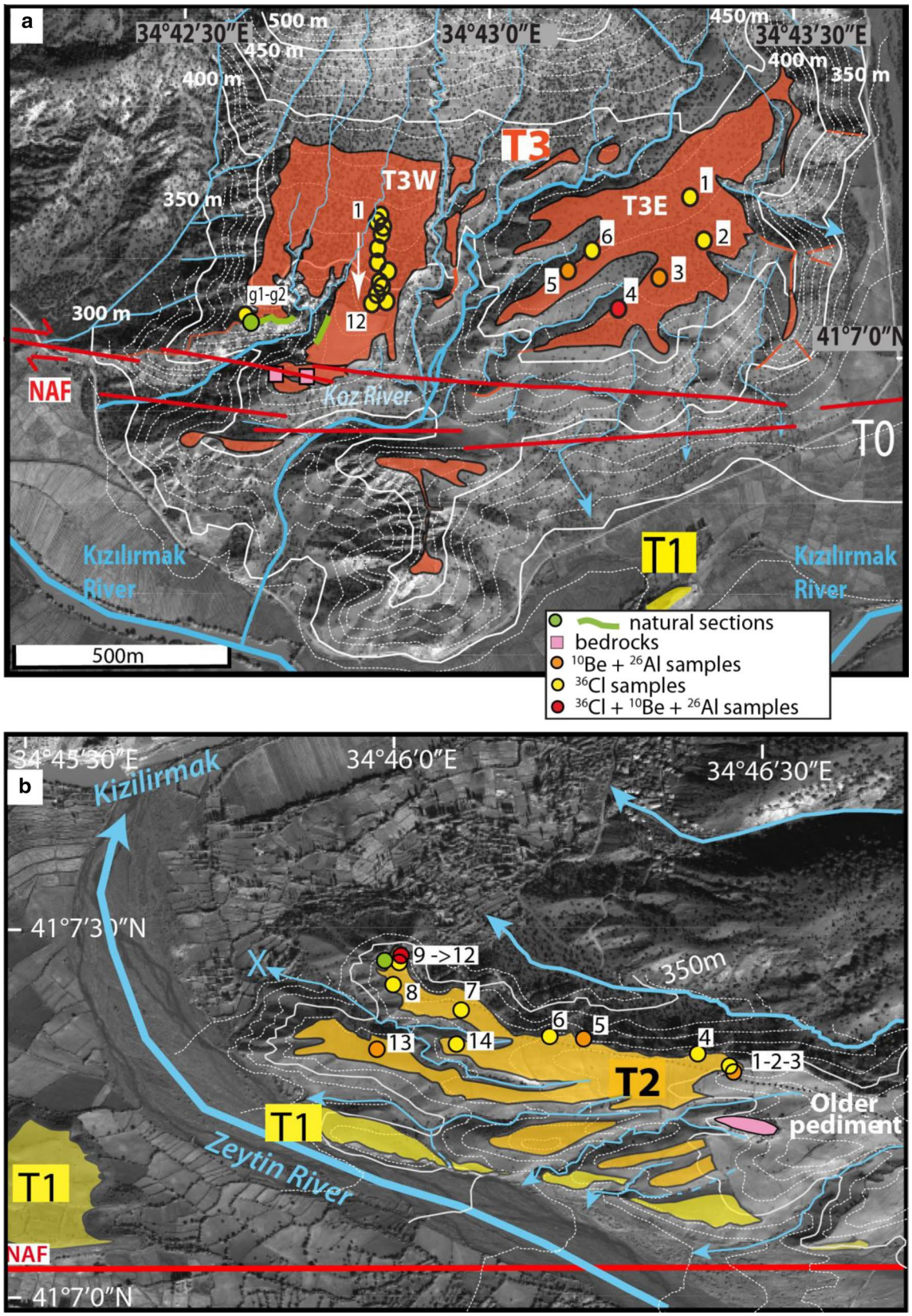
a
34°42'30"E
34°43'0"E
34°43'30"E
500 m
450 m
400 m
350 m
300 m
T3
T3W
T3E
T0
T1
NAF
Koz River
Kızılırmak River
41°7'0"N
g1-g2
natural sections
bedrocks
10Be + 26Al samples
36Cl samples
36Cl + 10Be + 26Al samples
500m
b
34°45'30"E
34°46'0"E
34°46'30"E
Kizilirmak
41°7'30"N
41°7'0"N
X
9 ->12
8
7
6
5
4
13
14
1-2-3
350m
T2
T1
Older pediment
Zeytin River
NAF

◂**Fig. 4** T3 and T2 strath terraces with topography on an Ikonos image and location of cobbles samples used for cosmogenic nuclide dating. **a** T3 mapping. Locations of the visible thin alluvial cover above the strath are indicated in green (see photo in Fig. 2d), and green circle for locations of the sampled depth section presented in the appendix (Figure S1a in the Appendix). **b** T2 limited to the east by a marble bedrock in pink; gully labeled X in Fig. 2d is indicated. Location of the visible thin alluvial cover above the strath because of a road cut, is indicated with green circle and corresponds to the sampled section for cosmogenic dating presented in the appendix (Figure S1.b). The fill terrace **T1** is mapped

isotopic ratios were also measured by accelerator mass spectrometry (AMS) at the ASTER AMS French national facility (CEREGE, Aix-en-Provence).

To compute Holocene catchment-averaged erosion rates from the ^{10}Be–^{26}Al concentrations (Table S1), we use the CAIRN method (Mudd et al. 2016) that calculates production and shielding on a pixel basis. We used as input (1) the 90 m-SRTM Digital Elevation Model for all catchments except the Kızılırmak one, and (2) the same parameters (production, half-life) as for the terrace samples and a rock density of 2.4. To compute paleo-denudation rates from sand in paleochannels, we use the methodology of Fuller et al. (2009) and took into account the post-depositional production of ^{10}Be.

3.2 Denudation rates of the CP

The erosion rates based on ^{10}Be–^{26}Al concentrations are listed in Table 1. The rates obtained are generally higher than the average worldwide drainage erosion rate [i.e., 218 m/Ma in Portenga and Bierman (2011)].

Regarding the Kızılırmak River, its average erosion rate is weakly constrained to 380 m/Ma, but our data imply a minimum erosion rate of 160 m/Ma, which is 3 times higher than the 50–60 m/Ma inferred on the Central Anatolian Plateau (Çiner et al. 2015). The low erosion rate on the plateau might be related to its increase aridity with respect to its border. The Anatolian Plateau has an average rainfall of 200–600 mm/year; whereas, the CP receive an average rainfall between 300 and 1200 mm/year. The compilation of ^{10}Be erosion rate data shows that arid region drainage basins tend to erode more slowly than others (Portenga and Bierman 2011). However, Von Blanckenburg (2006) argues that denudation rate in basins having a similar granitic geology strongly falls only below a rainfall threshold of 200 mm/year. The more arid climate of the Anatolian Plateau may, thus, not be the cause of its lower denudation rate. Another factor is tectonics. The CP are actively uplifting, whereas the Anatolian Plateau is mostly stable (e.g., Reilinger et al. 2006), and denudation is correlated with tectonics (Von Blanckenburg, 2006; Portenga and Bierman 2011) because of the strong control of tectonics over rock weathering (Edmont and Huh 1997). Therefore, we infer that the higher denudation rates in the CP compared to the Central Anatolian Plateau are linked to its active deformation and its related higher relief.

The Kızılırmak tributaries in the CP Range have an average ^{10}Be computed rate of 395 mm/ka, which is of the same magnitude as the Kızılırmak River (Table 1). Catchments show a large range of erosion rates. The highest rates occur in the N–S-oriented catchments directly affected by thrust faulting: i.e., L1, Bağyüzü (482 ± 120 m/Ma), L6 (710 ± 170 m/Ma) and L8 (324 ± 67 m/Ma) across the Tosya Basin and L10 (514 ± 191 m/Ma) across the Ilgaz Basin. L6, at the eastern end of the Tosya Basin, also has a headwater located in easily erodible ophiolitic rocks and has one of the steepest river gradients (Fig. 3). The lowest rate concerns the Zeytin catchment, L2 (134 ± 36 m/Ma). It may be surprising given that it strikes along the NAF, which would have damaged rocks close to its main strand potentially enhancing erosion. Its lower erosion rate might be related to the strong perturbation induced by large active landslides affecting its catchment and to the absence of active thrusts. The east–west-oriented Devrez River shows a denudation rate of 220 mm/ka that is lower than its northern tributaries. The later are crossed by the NAF and by active thrust and folds, and are limited by the high peaks of the Ilgaz Mountains (Figs. 1, 3). The Devrez catchment has a lower denudation rate than these tributaries probably because it has a lower mean slope and is sampling, on average, lower and less actively deforming ranges. Our results, thus, suggest a strong tectonic control of the denudation rates in CP and in Anatolia, as documented elsewhere in the geological record (i.e., Armitage et al. 2011).

^{26}Al measurements obtained from two former river beds in T2 and T3 (Fig. 4 and S1; Table 1 and S1) when corrected of post-depositional production of ^{26}Al gave very low concentrations ranging from 27,000 to 10,000 at/g. These measurements suggest that the denudation rates during the Last glacial period were larger than during the Holocene. Higher denudation rates may be related to an increase in physical weathering in the mountainous regions during cold period (e.g., Hales and Roering 2007; Matsuoka 2008; Fuller et al. 2009; D'Arcy et al. 2017). This mechanism was suggested in particular regarding in the carbonate mountainous regions in the Mediterranean area (i.e., Benedetti et al. 2002; Tucker et al. 2011).

4 Strath terraces in the Kamil Basin

4.1 Geomorphologic mapping

Along the Kızılırmak River, two sets of strath terraces are present above the floodplain (Fig. 2) (Fraser et al. 2010a).

Terraces were mapped according to their height above the Kızılırmak River, **T3** being the highest one, and **T2** the lowest one (Fig. 2c). Both are located at the western end of the Kamil pull-apart and show a similar very thin alluvial cover (Fig. 2d, Figure S2) visible only locally (Fig. 4).

T3 is located west of the ~ 1 km pull-apart basin at the confluence between the Zeytin and the Kızılırmak Rivers (Fig. 2a) (Fraser et al. 2010a). It stands 95 m above the Kızılırmak floodplain and is cut by the NAF (Figs. 2c, 4a). To the south of the NAF, two eroded **T3** remnants are identified. To the north of the NAF, **T3** is composed of two different surfaces with a 3.5° slope, separated by the Koz ephemeral stream. The eastern **T3E** surface is deeply incised and isolated because it surrounded by valleys and gullies. It is covered by few rounded pebbles and cobbles with a diverse lithology. In 2008, it was showing no trace of anthropic perturbations (agricultural fields or roads). Its well-rounded edges have no clear natural depth profiles. On the opposite, the western **T3W** surface is less incised and is in direct continuity with marble slopes to the north. It was slightly more modified in 2008: its southern part has been cleared for agricultural purpose. The surface is covered by numerous poorly rounded cobbles forming a nice pavement with a uniform marble lithology identical to the upslope relief (Fig. 2d). Natural depth sections are present along **T3W** vertical southern edge (Fig. 4a). The depth profile shows a 2–3 m thick alluvial deposits resting upon Pliocene marls (Figs. 2 and S1). The alluvial deposits are composed of thick packages of well-rounded cobbles/pebbles separated by few sandy layers.

T2 is located 75 m above the Kızılırmak floodplain (Figs. 2a, 4b). To the east, **T2** is connected to a marble bedrock outcrop and to a pediment (Figs. 2c, 4b). To the south, it is bounded by **T1** a younger very homogenous aggradational fill terrace (Figs. 2d, 4b). The **T2** surface is incised by gullies and is covered by cobbles having various lithologies. **T2** is more modified than **T3**: a road was built along its entire length and the surface was cultivated. Old field boundaries are marked by aligned cobbles and boulders. The clear contact between the strath and the alluvial cover is visible at only one location along the road cut. The depth profile at that location shows a 1.30 m thick fluvial deposit composed of polygenic pebbles as well as channels filled with clayed sand displaying cross-bedding structures (location in Fig. 4b and section in Figure S1). At the top, a debris flow deposit also locally stands ~ 1 m above the **T2** surface.

4.2 Deformation and terrace offsets

The Kamil Basin results from the occurrence of a ~ 1 km pull-apart basin at the confluence between the Zeytin and the Kızılırmak Rivers (Fig. 2a). West and east of pull-apart, the NAF is very linear and continuous (Fraser et al. 2010a). Across **T3**, it displays two parallel strands marked by numerous geomorphic features (Figs. 2, 4a). The southern strand is the main one; it is visible in section in the Koz stream and is associated with a flat pull-apart to the east of the Koz stream. It is linked with small stream offsets, captures and the larger offset of the Koz stream. The northern stand is evidenced by upslope facing scarps and by the deformation of **T3** forming a 1 m high north facing bedrock scarp to the west of the Koz stream (pink squares in Figs. 2a, 4a).

Two large cumulated right-lateral offsets are evidenced. First, the Koz ephemeral stream incising into **T3** shows an apparent right-lateral offset. Second, the **T3** eastern margins show a larger right-laterally offset; to the north–east, its margin corresponds to the valley of the Bağyüzü River. In the following, we discuss separately the two offsets and the associated piercing points used to assess the offsets considering the northern and southern fault strands.

Regarding the Koz offset, the eastern margin of T3W is right-laterally offset by the northern strand, as pointed out by piercing points *x* and *y* in Fig. 5. Defining the offset along the southern strand is less straightforward. To the south of the fault, the Koz incision trends N35E and is narrow. Piercing points a_2 and b_2 can be defined on both sides even if **T3** remnants are restricted and deformed. To the north of the NAF, the Koz stream and associated gullies have deeply incised **T3** with a similar N35E trend and form a relatively wide valley; piercing points, a_1 on the western side, and b_0 the eastern side can be defined (Fig. 5). The preferred reconstruction of the Koz stream incision corresponds to a cumulative displacement of 310 m and is displayed in Fig. 5b. It fully cancels the *S*-shape of the stream and partially erase the offset of T3E (see piercing point c_0/c_1 with c_2 on Fig. 5). Higher offsets would result in left-lateral deflection of the Koz stream across the fault.

The other offset concerns the eastern edge of the T3 terrace and is larger. The accuracy of the offset will not be optimal because it is eroded. North of the NAF, the piercing point can be defined following the T3 riser along the western edge of the Bağyüzü River. Close to the NAF, the Bağyüzü valley widens (Fig. 4a) and active aggradation occurs enhancing the preservation of the T3 riser. The later riser trends ~ N5E north and south of the NAF, so piecing points can be defined on both sides of the fault (Fig. 5). South of the NAF, two possible piecing points separated by ~ 130 m can be defined, bracketing the offset between 715 and 845 m. The reconstruction of T3 eastern edge also aligns the T3 western edge, south of the NAF, in front of the western margin of T3E, north of the fault. The Koz stream falls in front of a wide stream that has presently a small catchment north of the NAF insufficient to generate the stream power necessary to carve its deep and wide channel (Fig. 4a).

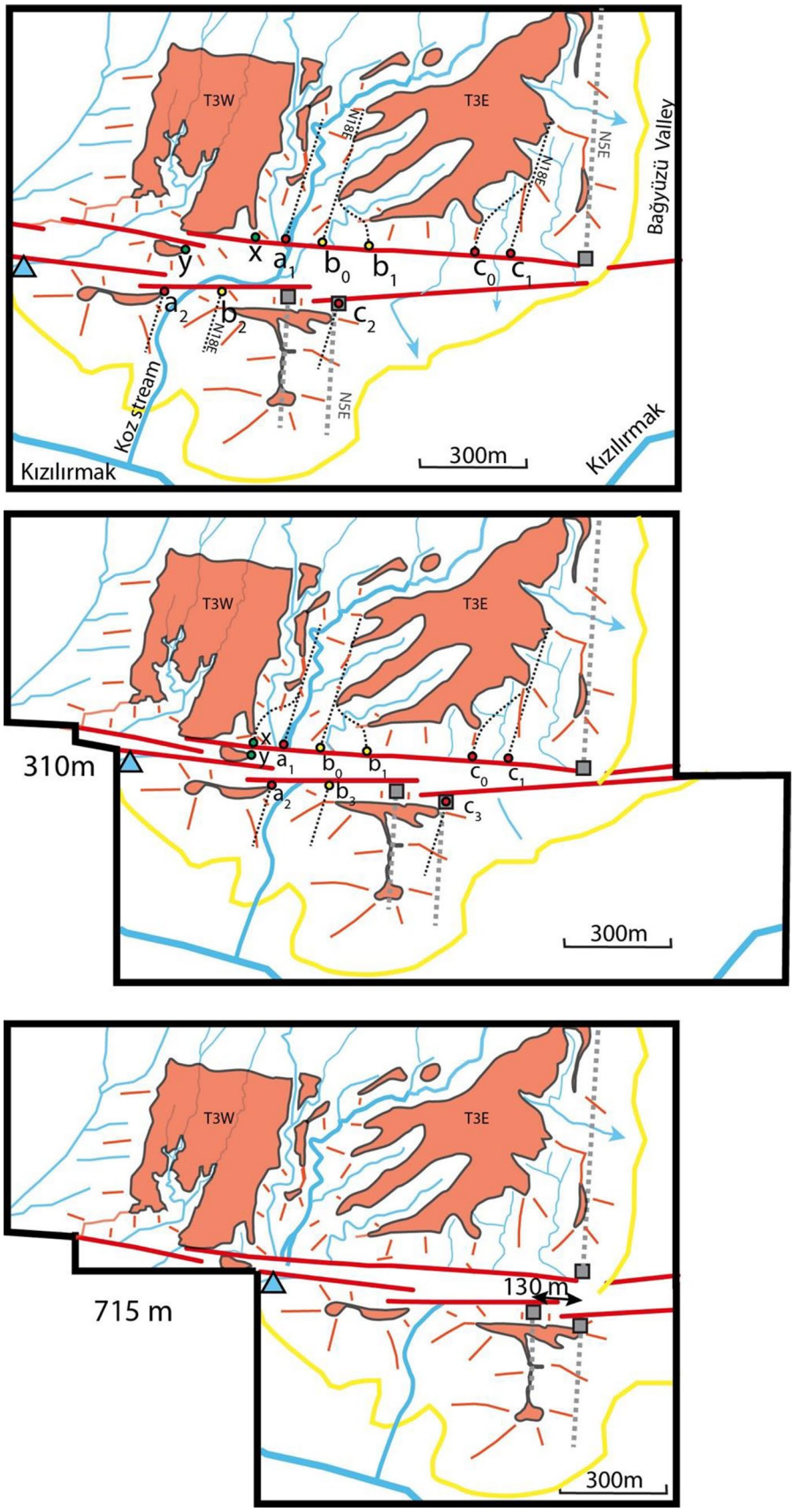

Fig. 5 Reconstruction of original geometry of T3 and of the Koz stream incising T3. **a** Present-day geometry with piercing points a_1–a_2 and b_0/b_1–b_2 on the two sides of the Koz stream used to reconstruct the initial Koz stream geometry; piercing points x and y evidenced T3 offset across the northern NAF strand. Small circles indicate piercing points for the reconstruction of the Koz river valley. Gray squares indicate piercing points for the reconstruction of the eastern edge of T3. **b** Reconstruction of the Koz initial geometry using a 310 m left-lateral offset along the NAF and the labeled round piercing points a and b of the Koz valley. **c** Reconstruction of the T3 eastern edge using a 715 m left-lateral offset along the NAF; the offset may be larger by 130 m as evidenced by the gray square piercing points. Blue triangle evidences the large river valley south of the NAF falling in front of the Koz valley north of the NAF

4.3 Cosmogenic dating

4.3.1 Terrestrial cosmogenic nuclide exposure dating

To constrain the **T2** and **T3** exposure history, an intensive examination of all terrace surfaces was performed to find quartz-rich cobbles to measure ^{10}Be and ^{26}Al, but mostly marble cobbles were found and sampled for ^{36}Cl measurements. Surface sampling was thus affected by the available cobble lithology. On **T3W**, only marble boulders and cobbles were found and marble cobbles were collected (Fig. 4a; Table S1). We took cobbles on the most preserved surface and away from gullies following a north–south profile (samples T3-1–T3-6, Fig. 4a). Additional samples (T3W-g1 and T3W-g2, Fig. 4a) were taken on the more eroded surface edge above the depth profile sampled (samples T3-sand-1–T3-sand-3 in Figure S1). On **T3E**, very few large samples were available. We collected three marble samples, two quartz-rich samples and one mixed sample with enough quartz and carbonates to quantify the three radionuclides ^{10}Be, ^{26}Al, and ^{36}Cl (Fig. 4a; Table S1). On **T2** and the associated debris flow, we collected seven marbles samples, two quartz-rich samples and four mixed samples with enough quartz and carbonates to quantify the three radionuclides (Fig. 4b; Table S1). **T2** was strongly modified: a road is running on it and old field boundaries made of aligned cobbles and boulders are visible. We sampled the surface along an east–west profile away from the road and fields (samples T2-1–T2-8, Fig. 4b), and to the south on the flattest surface remnants away from gullies and fields (samples T2-13–T2-14, Fig. 4b). We took surface samples of the debris flow locally covering the alluvial deposit at the western tip of the terrace edge (samples T2-9–T2-12, Fig. 4b) above the depth profile sampled for the evaluation of paleo-denudation rates (river sand samples T2-sand1 and T2-sand2 in Figure S1).We, thus, measured ^{36}Cl on marble surface samples, ^{10}Be, ^{26}Al on quartz-rich samples, and ^{10}Be, ^{26}Al, ^{36}Cl on mixed samples.

Regarding ^{10}Be and ^{26}Al dating, we followed the method of Kohl and Nishiizumi (1992). The samples were crushed, sieved, and cleaned to isolate the quartz-rich fraction. Quartz was isolated and purified by three progressive HF/HNO_3 leaches to each the exterior portion of the quartz crystal to remove atmospheric ^{10}Be and ^{26}Al that could have been adsorbed on the mineral surface (i.e., Brown et al. 1995). Acid-resistant and mafic minerals were removed from the residue leach by heavy liquid and/or magnetic separation. About 0.025 mg/g of ^{9}Be carrier was added to the purified quartz that was dissolved in HF. After dissolution, total ^{27}Al was measured in the sample solution by ICP-MS. ^{27}Al carrier is added if the total mass of ^{27}Al is less than 2 mg. Nuclide were chemically isolated during ion exchange columns. After precipitation, $Be(OH)_2$ and $Al_2(OH)_3$ were heated at 750 °C to obtain BeO and Al_2O_3. The ^{10}Be/^{9}Be and ^{26}Al/^{27}Al ratios were measured at the Accelerator Mass Spectrometer ASTER at CEREGE in France. Finally, the ratios were converted to ^{10}Be and ^{26}Al nuclide concentrations using the total Be and Al concentrations prior to chemical separation. Exposure ages were modeled using the CRONUS online calculator (Balco et al. 2008) version 2.2 (April 2009). We used ^{10}Be and ^{26}Al half-life [i.e., 1.387 Ma, see Korschinek et al. (2010) and Chmeleff et al. (2010); 708 ± 17 ka, see Nishiizumi (2004)], and the ^{10}Be, ^{26}Al production rates of Stone (2000), which show the lower variability from one area to an other (Lifton et al. 2014; Martin et al. 2017). Penetration depths used for age calculation of the few samples at depth profiles ages (see appendix) are 160 g cm^{-2} for neutrons and 1500 g cm^{-2} for muons (Granger and Smith, 2000; Gosse and Phillips 2001). We used a density of 2.7. No topographic shielding correction was needed given the extent and flatness of the terraces. Exposure ages were computed considering as a first hypothesis nul inheritance and erosion for all sample ages.

Regarding ^{36}Cl dating, we followed the procedure of Desilets et al. (2006). Samples were crushed, and the 250–500 µm fraction was isolated by sieving and then crushed. To calculate the different production ways of ^{36}Cl, a few g were sampled and the chemical compositions of bulk samples (major (Al, Ca, Fe, K, Mg, Mn, Na, P, Si, Ti) and trace elements) were measured by the Inductively Coupled Plasma-Optical Emission Spectrometry technique at the Service d'Analyse des Roches et des Minéraux (SARM), a CNRS laboratory in Nancy (France). Results are given in Table S4. Crushed samples were then leached and dissolved following the chemistry protocol of Stone et al. (1996). After complete dissolution of the crushed and leached samples, and the addition of a chlorine carrier, Cl is precipitated as AgCl. For the simultaneous Cl and ^{36}Cl determination by isotope dilution, samples are spiked with a known amount of isotopically enriched stable chloride carrier (Desilets et al. 2006). To track any Cl contamination in the chemistry process, a chemistry blank is coupled with each series of 10–15 samples and measured by AMS with its respective series. ^{36}Cl and chlorine concentrations were determined at the ASTER (CEREGE, Aix-en-Provence) facility in France. Analytical uncertainties (reported as 1σ) include uncertainties associated with accelerator mass spectrometry (AMS) counting statistics, AMS external error (0.5 per cent) and chemical blank measurements. Long-term measurements of chemically processed blank yield ratios are in the order of $(3.0 \pm 1.5)\ 10^{-15}$ (Arnold et al. 2010). ^{36}Cl exposure ages were modeled using the spreadsheet provided by Schimmelpfennig et al. (2009) with a neutron attenuation length of 160 g cm^{-2} (Gosse and Phillips, 2001) instead of 177 g cm^{-2} (Farber et al. 2008) to be self-consistent with the ^{10}Be model age calculations. Regarding spallation production rate from

Ca, we used the fact that we could measure ^{10}Be, ^{26}Al, and ^{36}Cl on the same sample to choose the most adequate spallation production rate for Ca. For that purpose, we also used another mixed sample (sample T1-6 in Tables S1, S2 and S3) coming from another **T1** fill terrace of the Kizimirlak River (N41.0836°; E34.4168°) highly impacted by anthropic activities (fields, road, etc.) for which we processed 6 surface samples (T1-1–T1-6) that gave ages ranging from 48.5 ± 5 ka to 550 ± 55 years and inconclusive age results (Table S2 and S3). We considered three production rates: 42.2 ± 4.8 atoms ^{36}Cl (g Ca)$^{-1}$ year^{-1} (Schimmelpfennig et al. 2011), 50 ± 5 atoms ^{36}Cl (g Ca)$^{-1}$ year^{-1}, 56 ± 5 atoms ^{36}Cl (g Ca)$^{-1}$ year^{-1} (Borchers et al. 2016). Only the spalliation rate of Borchers et al. (2016) gave consistent ^{36}Cl and ^{10}Be-^{26}Al ages for the six samples for which we got ^{36}Cl-^{10}Be-^{26}Al measurements over a time range of ~ 100 ka (Figure S3). We considered other factors like inheritance and erosion rates that could be responsible for the inconsistency between ^{36}Cl and ^{10}Be ages for a lower spallation production rate, but we could not identify another significant bias that you affect ^{36}Cl ages over 100 kyrs and that would not affect ^{26}Al ages that fully agree with ^{10}Be ages. We thus use a spallation rate of 56 atom (gCa)$^{-1}$ year^{-1} to model bulk ^{36}Cl ages (nul inheritance and erosion) in Table 2.

Table 2 ^{36}Cl samples: AMS results, model age (no inheritance, no erosion, density 2.7 for all samples). Sample locations in Table S1

Sample	^{36}Cl (measured)	Ages	
	(10^3 atoms. g^{-1} rock)	Age (years)	Error (years)
T3-1	3081 ± 61	102,221	11,842
T3-2	3402 ± 68	112,409	12,891
T3-4	2225 ± 44	71,547	8143
T3-6	2269 ± 45	78,278	8660
T3W-g1	925 ± 18	28,138	2934
T3W-g2	358 ± 7	11,115	1129
T3W-1	858 ± 19	25,581	2674
T3W-2	841 ± 19	28,007	2909
T3W-3	756 ± 17	23,082	2463
T3W-4	680 ± 15	21,061	2230
T3W-5	728 ± 16	23,191	2458
T3W-6	1063 ± 24	34,261	3677
T3W-7	720 ± 16	22,725	2404
T3W-8	1627 ± 36	50,891	5615
T3W-9	1423 ± 32	42,424	4615
T3W-10	1811 ± 40	56,331	6120
T3W-11	1298 ± 29	39,718	4329
T3W-12	1511 ± 34	49,078	5484
T2-1	1503 ± 30	50,926	5560
T2-2	1403 ± 28	43,019	4538
T2-3	1207 ± 24	36,705	3898
T2-4	3176 ± 63	107,048	12,108
T2-6	881 ± 17	26,914	2771
T2-7	1170 ± 23	38,299	4050
T2-8	2020 ± 40	66,816	7305
T2-9	916 ± 18	31,428	3336
T2-10	2312 ± 46	73,992	8509
T2-11	2389 ± 47	79,310	9861
T2-12	1394 ± 29	44,567	4591
T2-14	1449 ± 29	48,994	5334

The modeled ages are represented using density probability function to access the data dispersion and possible plurimodal distribution (Fig. 6). Following Brown et al. (2005), a pluri-modal distribution may indicate post-depositional reworking, and in that case the oldest ages may represent the age of the surface. On the opposite, a large dispersion may represent a variable inheritance, the youngest ages would have the smallest inheritance and would be representative of the terrace abandonment (e.g., Mériaux et al. 2005; Le Dortz et al. 2009). In the present paper, we discussed the geomorphologic processes at play on the terraces to interpret exposure dates (Applegate et al. 2012), and did not follow directly the previous interpretations.

4.3.2 Evaluation of erosion rates and inheritance

Possible corrections related to erosion rates need to be evaluated. We first critically assess erosional processes on the terraces. The former alluvial deposits visible in sections are mostly composed of cobbles with few coarse sand layers. Erosional processes on these surfaces would be driven by overland flow and deflation. Large overland flows can be erosive particularly during cold and arid glacial periods with a restricted vegetation cover, but cobbles are still likely to have a long residence on the inner flat part of the terrace. Deflation would affect only the finest particles, and concentrate the cobbles at the surface. This process would have a relative minor impact because the initial alluvial deposit is mostly composed of large particles (Figure S1). The erosion rate linked to these processes is, thus, likely to be minimal. On **T2**, cultivation has triggered the exhumation of buried cobbles and may have increased the erosion rate of the finer particles, but we are lacking any way to quantify these parameters.

Several additional constraints could be inferred. First, we had a specific strategy for minimizing the erosion bias (e.g., Van der Woerd et al. 2006). We sampled surface cobbles with 10 to 20 cm diameter that are less likely to be reworked compare to pebbles. We selected cobbles having a thick alteration ring on the upper-side and some dissolved features on the down-side. This alteration pattern implies that they had remained a significant time on the exposed surface and have not been recently bought to the surface by ploughing (Burbank and Anderson 2009). Second, we sampled the flat inner parts of the terraces where erosion

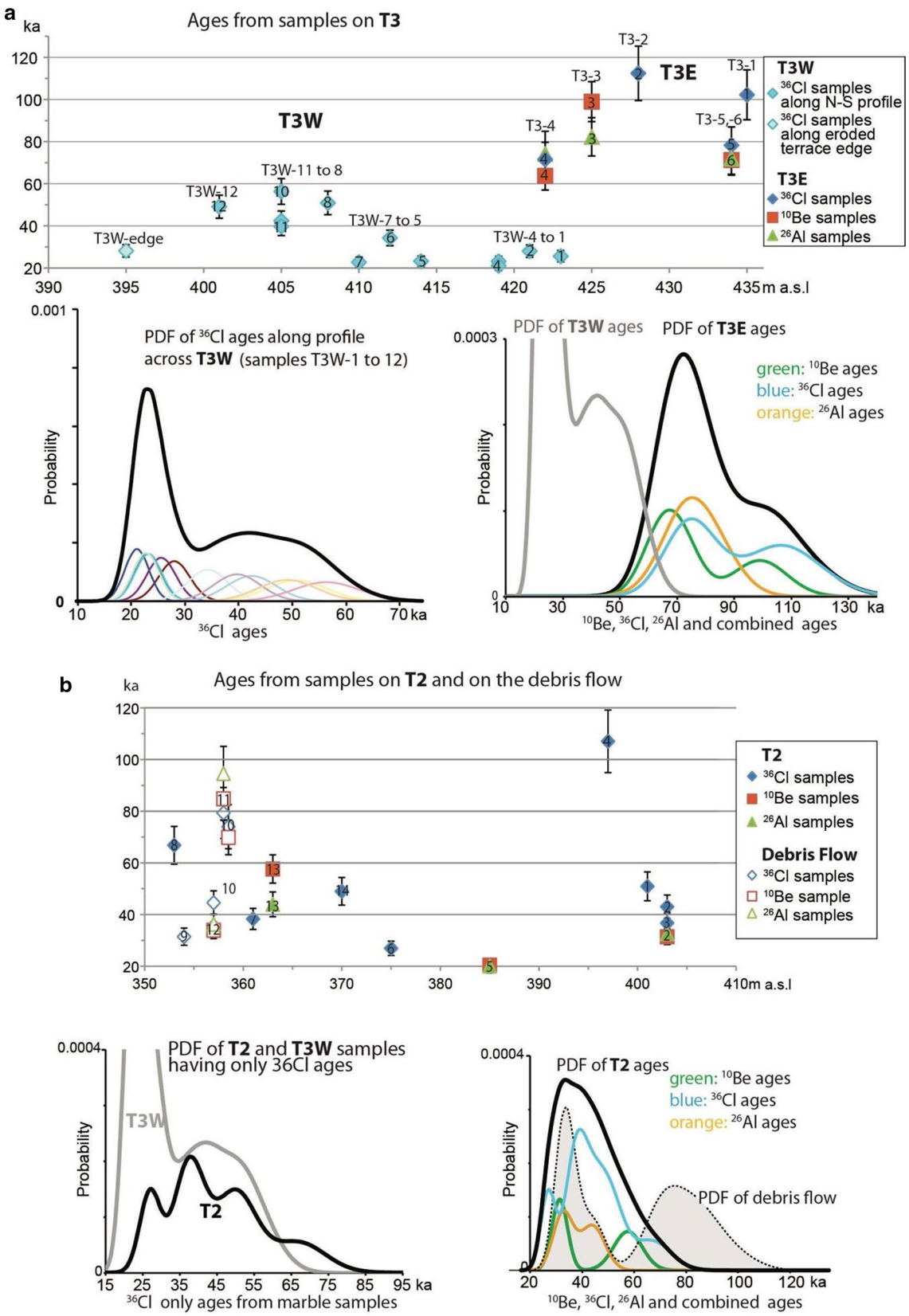
a
Ages from samples on T3
ka
T3W
T3E
T3-1
T3-2
T3-3
T3-4
T3-5,-6
T3W-edge
T3W-12
T3W-11 to 8
T3W-7 to 5
T3W-4 to 1
T3W
36Cl samples along N-S profile
36Cl samples along eroded terrace edge
T3E
36Cl samples
10Be samples
26Al samples
435m a.s.l
PDF of 36Cl ages along profile across T3W (samples T3W-1 to 12)
Probability
36Cl ages
PDF of T3W ages
PDF of T3E ages
green: 10Be ages
blue: 36Cl ages
orange: 26Al ages
10Be, 36Cl, 26Al and combined ages
b
Ages from samples on T2 and on the debris flow
T2
36Cl samples
10Be samples
26Al samples
Debris Flow
36Cl samples
10Be sample
26Al samples
410m a.s.l
PDF of T2 and T3W samples having only 36Cl ages
T3W
T2
36Cl only ages from marble samples
PDF of T2 ages
green: 10Be ages
blue: 36Cl ages
orange: 26Al ages
PDF of debris flow
10Be, 36Cl, 26Al and combined ages

◂**Fig. 6** T3 and T2 cosmogenic exposure ages. **a** *Top*: T3 exposure ages versus elevation above sea level (a.s.l.). *Bottom right*: probability density function (PDF) of ^{36}Cl exposure ages for samples T3W-1–T3W-12 following a north–south profile on the western surface (see location in Fig. 4a). *Bottom left*: probability density function of ^{36}Cl, ^{26}Al and ^{10}Be exposure ages for all samples the eastern T3 surface (T3E). **b** *Top*: T2 exposure ages represented versus elevation above sea level (a.s.l.). *Bottom left*: probability density function of exposure ages for T2 samples compared to T3W. *Bottom right*: probability density function of ^{36}Cl, ^{26}Al and ^{10}Be exposure ages for all T2 samples. Samples corresponding to the debris flow (T2-9–12) are identified separately

and anthropic perturbations were minimal. Erosion rates on flat surfaces, were likely to an order of magnitude smaller than the obtained averaged denudation rate around 200 m/Ma obtained using river sands. Finally, Yıldırım et al. (2013) based on ^{10}Be depth profile on a terrace inferred a possible erosion rate of 1 mm/ka in the nearby Gökırmak catchment. All these elements point to a low to negligible erosion rate of the inner part of the terraces.

The prior exposure is the other important bias, cobbles could have gained an initial concentration before their deposition on the terrace. To take into account this bias, we first did multiple sampling on the surfaces: 19 on **T3**, 11 on **T2** and 3 on **T2** debris flow above (Fig. 4). We also looked at inheritance obtained by Yıldırım et al. (2013) evaluated in the nearby Gökırmak catchment. They evaluated possible inherited ^{10}Be concentrations ranging from 140,000 to 40,000 atoms.g^{-1}. Similarly, Çiner et al. (2015) evaluated the inherited concentration in Kızılırmak terraces in the Central Anatolian Plateau between 0 and 15,000 to 25,000 atoms.g^{-1} on a 160 ± 30 ka terrace. Another way to assess the presence of inherited nuclides is to date the active riverbed (e.g., Hetzel et al. 2006). We obtained ^{10}Be concentration ranging from 10,000 to 50,000 atoms.g^{-1} in riverbeds. Finally, we used as sub-surface samples, the few sand samples collected in section across **T3** and **T2** for another purpose (i.e., paleoerosion denudation rates; Figure S1). The sub-surface concentrations were modeled by fitting the sample concentrations like in Granger and Smith (2000) and using the constant surface production rate determined by the CRONUS calculator. We tested different inheritance scenario within the 10,000–50,000 atoms.g^{-1} and the two profiles could be fitted with no inheritance or with a small one of 10,000 atoms.g^{-1}. We, thus, finally choose not to apply any systematic corrections for erosion and prior exposition.

4.4 Bulk ages

On **T3**, we distinguished the **T3E** from **T3W** because of their different surface characteristics (cobble lithology and pavement). On **T3E** surface, we obtained concordant ^{10}Be ages (99 ± 9–71 ± 7 ka), ^{26}Al ages (82 ± 9–64 ± 7 ka), and ^{36}Cl ages (112 ± 13–72 ± 8 ka) as displayed in Fig. 6a (Tables 1 and 2). We, thus, infer a simple exposure history. The PDF of the different nuclides are overlapping and are similar. All samples independently of their lithology have similar ages. The **T3E** average age is 83 ± 15 ka. On **T3W** surface, we obtained twelve ^{36}Cl ages along a north–south transverse, ranging from 21 ± 2 ka in the north to 56 ± 6 ka in the south, and two ^{36}Cl ages from samples more to the west close to terrace edge, i.e., T3W-g1: 28 ± 3 ka and T3W-g2: 11 ± 1 ka (Fig. 6a). This last sample is inconsistent with the others and considered an outliner. Representing the sample ages using probability functions, we identify two clusters. The youngest one comprises all samples located close to the hillslope; it is centered on 22 ka and spans the 20–31.5 ka period. The oldest cluster comprises samples located father south; it is centered on 42 ka covering the 31–58 ka period (Fig. 6). All exposure ages are younger than on **T3E** surface (Fig. 6a). The age differences between **T3W** and **T3E** imply that specific geomorphic processes are at play on **T3W**. We discuss this topic in the next section.

On **T2**, the ^{10}Be and ^{26}Al ages overlaps with ^{36}Cl ages, and we identified two outliners: T2-4 with an age of 107 ± 12 ka and T2-5 with an age of 20 ± 2 ka (Fig. 6b; Tables 1 and 2). Removing them, we obtained a PDF for **T2** ranging from 24 to 64 ka with a maximum at 34 ka. When we plot the PDF of the ^{10}Be, ^{36}Cl and ^{26}Al ages, we obtain similar age ranges. In addition, **T2** ages are similar to **T3W** ages, even though terraces have different heights**.** When we plot PDFs of **T2** ^{36}Cl ages and of **T3W** ^{36}Cl ages from marble samples, we have a nearly complete overlap, which implies a similar exposure history.

For surface samples of the debris flow on **T2** edge, we obtained different ages: 31 ± 3 ka (^{36}Cl ages) for T2-9, 70 ± 7 ka to 74 ± 9 ka (^{10}Be and ^{36}Cl ages) for T2-10, 85 ± 8 ka, 95 ± 11 ka, 79 ± 10 ka (^{10}Be, ^{26}Al and ^{36}Cl ages) for T2-11 and 34 ± 3 ka, 36 ± 4 ka, 45 ± 5 ka (^{10}Be, ^{26}Al and ^{36}Cl ages) for T2-12 (Fig. 6b; Tables 1 and 2). The PDF evidence two clusters: the first one with maxima around 78 ka, an age similar to **T3E,** and the second around 34 ka. The wide age spread in the debris flow is probably related to the fact that it reworked already exposed cobbles. The old cluster spanning the 70–95 ka period is interpreted as representing reworked materials with a prior exposure. The youngest cluster with ages between 30 and 44 ka would correspond to the emplacement age of the debris flow. We infer that **T2** must be older this youngest cluster.

4.5 Terrace ages, age spread and the inferred frost-cracking process

The simple age distribution of the isolated **T3E** surface contrasts with the age span of **T3W** (21–56 ka range) and **T2** (24–64 ka range) connected to the hillslope (Fig. 6). The large number of exposure ages still allows for identification

of probable geomorphological processes responsible for **T2** and **T3W** broad overlapping age spread.

The **T3** surface, which is the most preserved regarding anthropic modifications, shows the clearest pattern. The **T3** cobbles located west and east of the Koz ephemeral stream belong to the same surface (Figs. 2, 4a), but have different exposure ages (Fig. 6a). So, different geomorphological processes were at play on these surfaces. The younger exposure ages on the **western T3** surface are, thus, interpreted to reflect hillslope processes during the Glacial Period, posterior to the terrace bevelling and entrenchment. We propose the following interpretation of the **T3W** age distribution. We consider that the surface acts as a pediment in direct connection with a carbonate hillslope as displayed in the sketch in Fig. 7. Marbles cobbles on the **T3W** surface that form a pavement are interpreted to come from the hillslope and result from frost-cracking acting on the marble bedrock. During cold intervals, frost-cracking is a dominant erosional process on carbonate and marble hillslopes of the Mediterranean area (Anderson et al. 2013). This specific process at play was evidenced around the Mediterranean during the Glacial Period (Tucker et al. 2011). It leads to a larger degradation of carbonate slopes during the Glacial Period compared to the Holocene (e.g., Armijo et al. 1992; Piccardi et al. 1999; Morewood and Roberts 2000). The cobbles resulting from this process would cover the original alluvial deposit.

Frost-cracking is not a continuous process. Its intensity depends on two main variables: first, the time spent in the frost-cracking window (ranging from −8 to −4 °C) and second, the water availability directly linked to Winter/Spring precipitation (Anderson and Anderson 2010). A cold and humid climate would be much more favorable than a cold and dry one. High-resolution pollen data from the southern Black Sea cores record vegetation changes in the CP (Mudie et al. 2007; Shumilovskikh et al. 2012, 2013, 2014) and attest for the occurrence of large changes in temperature and humidity implying that frost-cracking would not be a steady phenomena (Anderson et al. 2013). The two age clusters at 23–2 + 3 ka and between 40 and 55 ka on **T3W** surface correspond to the two coldest intervals during the last 135 ka in the CP (see Badertscher et al. 2011), and particularly to the two more humid periods identified using pollen data around 45–54 ka and 20–28 ka in the CP (Langgut

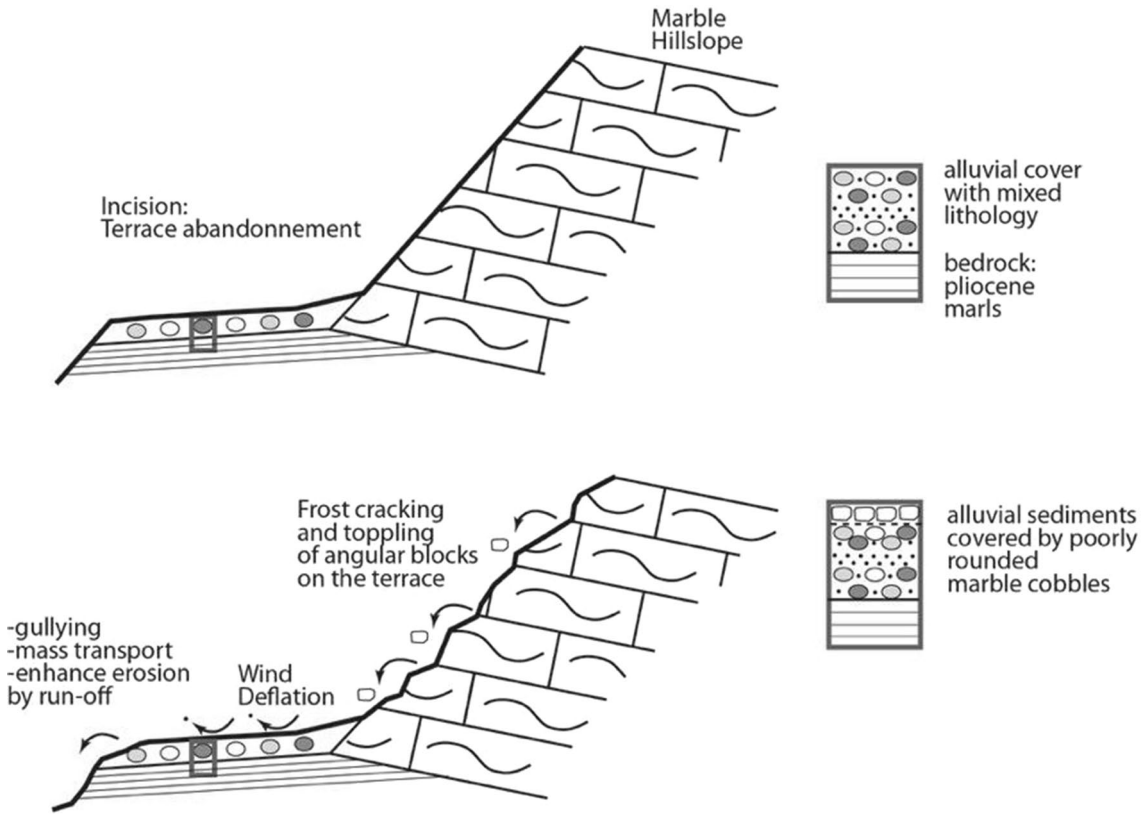

Fig. 7 Sketch displaying the geomorphological processes at play in a cross-section since terraces incision and abandonment (top diagram): the terrace surface acts as a pediment (bottom diagram) where new marble cobbles are supplied by episodic frost-cracking by the hillslope, and are in transit on the surface; on the right, typical sedimentary sections across the terraces. Frost-cracking process results in covering the original alluvial sediment by a marble cobble pavement

et al. 2011; Shumilovskikh et al. 2014). These more humid phases correspond to glacial advances in Turkey. The first one fits the 53–44 ka glacial advance (Reber et al. 2014) in Eastern Black Sea Mountains in Turkey, and the second one, the better known Last Glacial Maximum (LGM) advance in Turkey. The LGM in Turkey is characterized by cooler temperature and a doubling in precipitation at 22 ± 4 ka in comparison with the previous period (Akçar et al. 2014; Reber et al. 2014).

The age distribution along the north–south profile on **T3W** surface would, thus, be related to periodic frost-cracking and downslope transport. Frost-cracking during cold and humid periods would degrade hillslopes and provide new carbonate cobbles on the upslope part of the surface, the last episode being the LGM. The cobbles would be slowly transported downslope when large overland flow occurred like in any pediments. So, older marble cobbles would be found farther away from the slope. This geomorphological scenario is consistent with the exposure ages obtained along the profile across **T3W** (T3W-1–12; Fig. 4a): many LGM carbonate cobbles are found near the hillslope and there is a trend toward older ages away from the hillslope (Fig. 6a).

These processes also provide an explanation for the numerous carbonate cobbles present on **T3W** forming a pavement (Fig. 2e) and the few older cobbles with a mixed lithology found on **T3E**. **T3E** and **T3W** have different histories because **T3E** surface is separated from the hillslope by a gully system forming the head catchment of the Koz stream (Fig. 4a), so **T3E** is disconnected from the hillslope. **T3** abandonment and incision can, thus, only be inferred using samples on the eastern surface. We obtain an age of 83 ± 15 ka by averaging **T3E** ^{10}Be and ^{36}Cl exposure ages. The age obtained is compatible with ^{10}Be and ^{326}Al exposure ages at depth in **T3** (Table 1; Figure S1).

On **T2**, we observed a ^{36}Cl ages distribution similar to **T3W**. So frost-cracking is also likely to be present because part of the **T2** surface is in continuity with a pediment, carbonate bedrock, and carbonate slopes (Figs. 2c, 4b). Indeed, ^{36}Cl ages belonging to the two main frost-cracking periods, LGM (T2-6: 27 ± 3 ka) and 40–55 ka (T2-1: 51 ± 6 ka, T2-7: 38 ± 4 ka, T2-14: 49 ± 5 ka), are also present on the **T2** surface (Fig. 6b). Another process is also probably at play. Human ploughing, which leads to younger exposure ages for exhumed cobbles, is a probable bias, even if we sampled away from visible fields and selected cobbles with a large alteration ring.

Given these two potential bias, we consider that samples most representative of **T2** age should be the oldest samples and should come from an isolated terrace remnant. In addition, **T2** bevelling must be (1) older than the debris flow emplaced around 30–44 ka, and (2) younger than **T3**. Given these constraints, sample T2-8 (66.8 ± 7.3 ka), that comes from a surface surrounded by deep gullies, is considered the best to represent the terrace age. This age is also coherent with cosmogenic concentrations we have at depth in **T2** profile (Table 1; Figure S1).

5 Fill terraces in the Kamil Basin

5.1 Geomorphologic mapping

In addition to the strath terraces**,** two aggradational fill terraces, **T1** and **T0,** are observed in the Kamil Basin. The **T1** thick aggradation fill is prominent near the intersection of the Zeytin and the Kızılırmak Rivers (Figs. 2, 4b). The homogeneous ~ 20–25 m thick fill shows no major discontinuity and no paleosoil formation. These observations suggest that it was deposited over a short period of time, sometime after the incision and abandonment of **T2** and **T3**. The aggradation fill is visible at other locations along the ~ 30 km section of the Kızılırmak River between the Kamil and the Kargı pull-aparts (Fig. 1a). At that location, cosmogenic dating provides inconclusive ages (Tables S2 and S3 in the Appendix).

The lower **T0** aggradational fill stands a few meters above the floodplains of the Kızılırmak, Zeytin, and Bağyüzü Rivers in the Kamil pull-apart (Fig. 8). It was deformed during the 1943 earthquake according to local witnesses. It is flooded since the construction of a dam on the Kızılırmak River, and is no more visible.

5.2 Terrace offset

T1 remnants are dispersed and do not form a continuous surface that can be used to constrain strike-slip motion along the NAF. **T1** is locally deformed close and south to the NAF, but its deformation pattern was not investigated here.

On the opposite, **T0** show a clear offset**,** just east of **T3**, where a single NAF strand can be mapped (Figs. 2a, 8a). **T0** is farmed and stands ~ 3 m above the ~ 100–200 m wide Bağyüzü floodplain (Fig. 8a, d). It is crossed by a fresh 0.5–1 m a continuous south-facing scarp (Fig. 8c). Close to the river, **T0′** is an additional inset paired terrace; it stands 1–2 m above the riverbed and has preserved **T0** from erosion (Figs. 8a, d).

To characterize the fault deformation, we measured the terrace riser between **T0** and **T0′** as well as the T0′ edge using a total station. Theodolite profiles show that the floodplain is warped (Fig. 8d). On the western side of the river, the **T0–T0′** riser is protected from active river erosion and records a cumulated right-laterally offset of 14 ± 2 m based on theodolite measurements (Fig. 8b). The maximum uncertainties inferred are linked to the shape riser. T0′ shows a possible right-laterally offset of 2 m, identical to the 1943 earthquake slip documented at that location (Barka 1996).

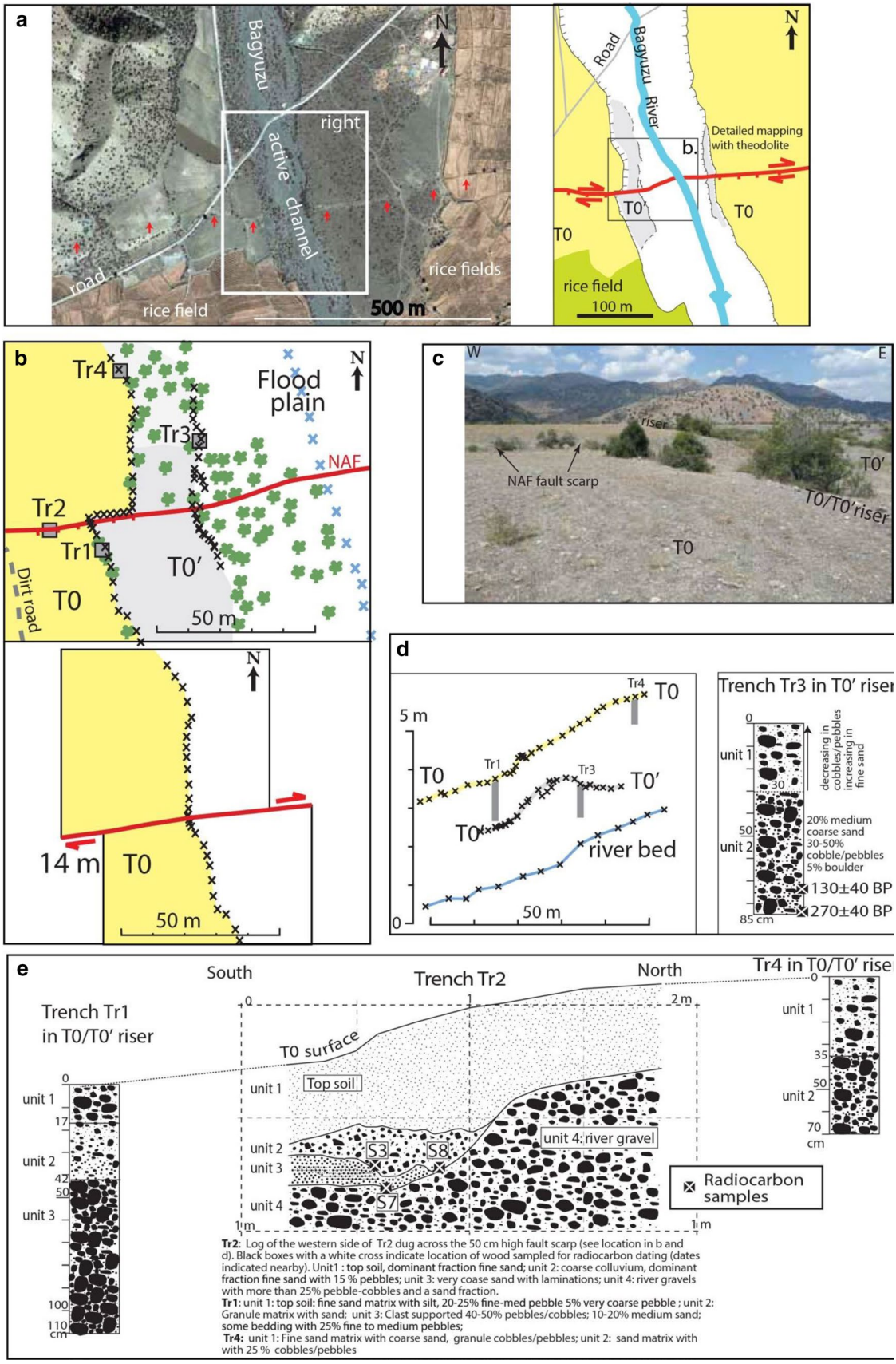

Tr2: Log of the western side of Tr2 dug across the 50 cm high fault scarp (see location in b and d). Black boxes with a white cross indicate location of wood sampled for radiocarbon dating (dates indicated nearby). Unit1 : top soil, dominant fraction fine sand; unit 2: coarse colluvium, dominant fraction fine sand with 15 % pebbles; unit 3: very coase sand with laminations; unit 4: river gravels with more than 25% pebble-cobbles and a sand fraction.
Tr1: unit 1: top soil: fine sand matrix with silt, 20-25% fine-med pebble 5% very coarse pebble ; unit 2: Granule matrix with sand; unit 3: Clast supported 40-50% pebbles/cobbles; 10-20% medium sand; some bedding with 25% fine to medium pebbles;
Tr4: unit 1: Fine sand matrix with coarse sand, granule cobbles/pebbles; unit 2: sand matrix with with 25 % cobbles/pebbles

◂**Fig. 8** T0 and T0′ aggradational terraces offset by the NAF. **a** *Left*: Ikonos image of the site, showing the NAF cutting the Bağyüzü active river bed and older alluvial terrace deposits; fault scarp facing south are marked by black arrows; box indicates location of figure to the right. *Right*: geomorphological map with T0 in yellow and T0′ in gray; box indicates location of (**b**). **b** *Top*: map of T0 and T0′ on the river western side. Risers and riverbed were measured in the field with a theodolite (i.e., crosses: individual measurements); gray squares indicate trench locations. *Bottom*: reconstruction of a straight T0 riser using a back left-lateral motion of 14 m; T0/T0′ riser is offset by about 2 m. **c** Photo of the offset T0/T0′ riser and of the fault scarp. **d** *Left*: theodolite profiles projected north showing T0 and T0′ relative heights with respect to the riverbed; trenches location indicated. *Right*: log of Tr3 in T0′ riser and ^{14}C ages obtained. **e** Trenches across T0. *Middle*: log of the Tr2 western side across the 50 cm high scarp; black boxes with white cross indicate location of wood samples for radiocarbon dating (dates indicated in the text). *Left*: Tr1 log. *Right*: Tr4 log

The low slip in the Kamil area during the 1943 earthquake was also documented by a water channel offset in the nearby Alibey village located 12 km East of Kamil (Figure S2 in the Appendix).

5.3 Terrace stratigraphy and earthquake deformation

In **T0**, four ~ 1 m deep trenches were excavated to constrain the stratigraphy, deformation and age of the terraces (Fig. 8b, d, e). Tr2 is our reference trench; it was dug across the fault scarp; Tr1, Tr3 and Tr4 were dug in the risers. In all trenches, the bottom unit (unit 4 in Tr2, unit 3 in Tr1, unit 2 in Tr3 and Tr4) contains more than 25% of pebbles/cobbles, and a significant sand fraction like the present floodplain deposit (Fig. 8d, e). These coarse grain-size riverine deposits are overlain by finer grained units with a sharp contact in **T0** (Tr1, Tr2, Tr4) and a gradational contact in **T0′** (Tr3). The transition between the two units is interpreted to correspond to the river incision resulting in the terrace formation. The finer grained units would result from (1) flood events, (2) deflation that reworks floodplain sands and transport them on the terrace surface, and (3) agricultural practices. The grain-size variations in top units in trenches may related to agricultural practices: cobbles would be removed from the main surface (i.e., Tr2) and stored near the risers (i.e., Tr1).

In trench Tr2 across the **T0** scarp, the folding of riverine unit 4 is about twice more important than the warping of unit 1. We thus infer that the scarp results from at least two deformational episodes (Fig. 8e). Deformation of unit 1 is nearly uniform with similar deformation at its base and top. Unit 1 is a uniform top soil resulting from agricultural practice that have destroyed any evidence of faulting. Below in river gravels of unit 4, no distinct fault trace could be identified due to Tr2 low depth and to the difficulty of identifying faults in gravels. Two additional units are present on the down-through side of the scarp. The unit 3 is a finer grained unit with coarse sands and laminations, and the overlying unit 2 is a coarse wedge composed of 15% pebbles in a fine sandy matrix. We interpreted unit 2 as a colluvium, and unit 3 as an over-bank deposit on top of the river gravels (i.e., unit 4).

5.4 Dating and earthquake occurrence

T1 terrace was sampled in the Kargi Basin for cosmogenic dating, which provides inconclusive results (Table S3).

In **T0** and **T0′**, the deposition chronology was constrained by radiocarbon dating. Regarding **T0′**, the wood sample at Tr3 bottom gave a calibrated age using Oxcal and the INTCAL13 calibration curve with an 86% probability of occurrence during the 1486–1676 A.D. period (Fig. 8d). In **T0** and Tr2, there were two large wood samples, S3 and S8, at the base of the colluvial unit 2 (Fig. 8e). Their respective calibrated ages imply a 70.5% probability of occurrence during the 1805–1931 A.D. period and a 70.5% probability of occurrence during the 1810–1926 A.D. period. These large wood fragments trapped by colluvium are slightly older than the 1943 earthquake. The S7 small sample was collected at the boundary between the over-bank unit 3 and the river gravel unit 4 to constrain the **T0** incision We obtain a calibrated age with a 95% probability of occurrence during the 1455–1638 AD interval. Unit 4 was, thus, deposited before the 1668 earthquake.

The stratigraphy and the calibrated ages suggest that the **T0** terrace history is in relation with the two last earthquakes rupturing the central NAF in 1943 A.D. and 1668 A.D. (Barka 1996). **T0** has been incised and abandoned shortly before the penultimate AD 1668. The earthquake warped the terrace and offset unit 4 in Tr2. In this scenario, the 1668 A.D. event horizon would be at the top of unit 4 or associated with unit 3. **T0′** that is younger than **T0** may have been deposited shortly after the 1668 earthquake, in relation with river aggradation potentially related to a post-earthquake increase in sediment discharge like in Taiwan (Dadson et al. 2004). Its deposition preserved the **T0** offset. Colluvial unit 2 was deposited close to the 1943 earthquake. The ^{14}C ages suggest that it is older, but the large wood samples may have inherited or inbuilt ages and may not have capture the capture the actual age of the deposit (Streig et al. 2020).

Tr2 stratigraphy and dating also imply that the 14 ± 2 m **T0/T0′** riser offset results from the cumulated ruptures of the 1943 and 1668 earthquakes. The cumulated displacement is similar to the 15.5 m of right-lateral displacement of large old water canal built before the 1943 earthquake in the village of Alibey, located 12 km to the east of the investigated site (see Figure S2 in the Appendix). There are few other co-seismic slip measurements about both earthquakes. The 1943 co-seismic slips of 1.4 and 2.6 m were measured at two locations near Kamil (Barka 1996). These ~ 2 m historical offsets imply that the 1668 A.D. surface slip was greater than

10 m in Kamil. Fraser et al. (2010a) also inferred a probable 10 m slip during the 1668 earthquake at the Elmacik trench site ~ 10 km east of Kamil and Sugai et al. (1999), a 5–6 m offset in Ilgaz, ~ 60 km west of Kamil. Much farther east on other fault segments, several studies also evidenced large slip during the 1668 earthquakes (Kondo et al. 2010; Zabcı et al. 2011; Hubert-Ferrari et al. 2012). This larger offset is in agreement with the longer rupture and larger magnitude of the 1668 earthquake (Ambraseys and Finkel 1988). The displacement per event along the central NAF is, thus, variable between seismic cycles, as already suggested by Fraser et al. (2010a,b), a behavior not observed along the 1944 segment further west (Kondo et al. 2010).

6 Discussion

6.1 Terrace deposition, incision and possible climate-related formation

The following hillslope and fluvial processes were at play in the Kamil pull-apart over the last 120 kyrs. Frost-cracking during the humid and cold periods strongly affected the carbonate and marble hillslopes and delivered cobbles downstream to pediments, terraces and rivers. Two episodes of strath planation followed by incision occurred leading to the formation of terraces **T3** and **T2**. Finally, a large sedimentary infill occurred as attested by the **T1** and **T0** fill terraces that were subsequently incised. The terrace formations are likely to be influenced by two main factors: the climate changes characterizing the last 130 kyrs and the base-level change. The studied site is located ~ 90 km away from the Black Sea and water level changes of the Black Sea, that are partly decoupled from global sea level changes (Panin and Popescu 2007; Krijgsman et al. 2019), are likely to play a role in the river aggradation and incision. This control was pointed in the case of the Danube River (Armaş et al. 2019) and the Sakarya River (Erturaç et al. 2019) among others. The possible origin of the different terraces in Kamil is discussed in the following.

The **T3** strath terrace standing 95 m above the present river bed indicates river incision triggered by tectonic uplift. The 83 ± 15 ka age of **T3** is consistent with ages of strath terraces (81 ± 8 ka and 99 ± 8 ka ^{10}Be ages and 78 ± 7 ka ^{36}Cl age) and pediments (70 ± 7 ka ^{21}Ne age) in the Gökırmak River, a tributary of the Kızılırmak River (Yıldırım et al. 2013a) (Fig. 9). More to the west, a strath terrace with an 88 ± 5.1 ka age was also mapped along the Filyos River

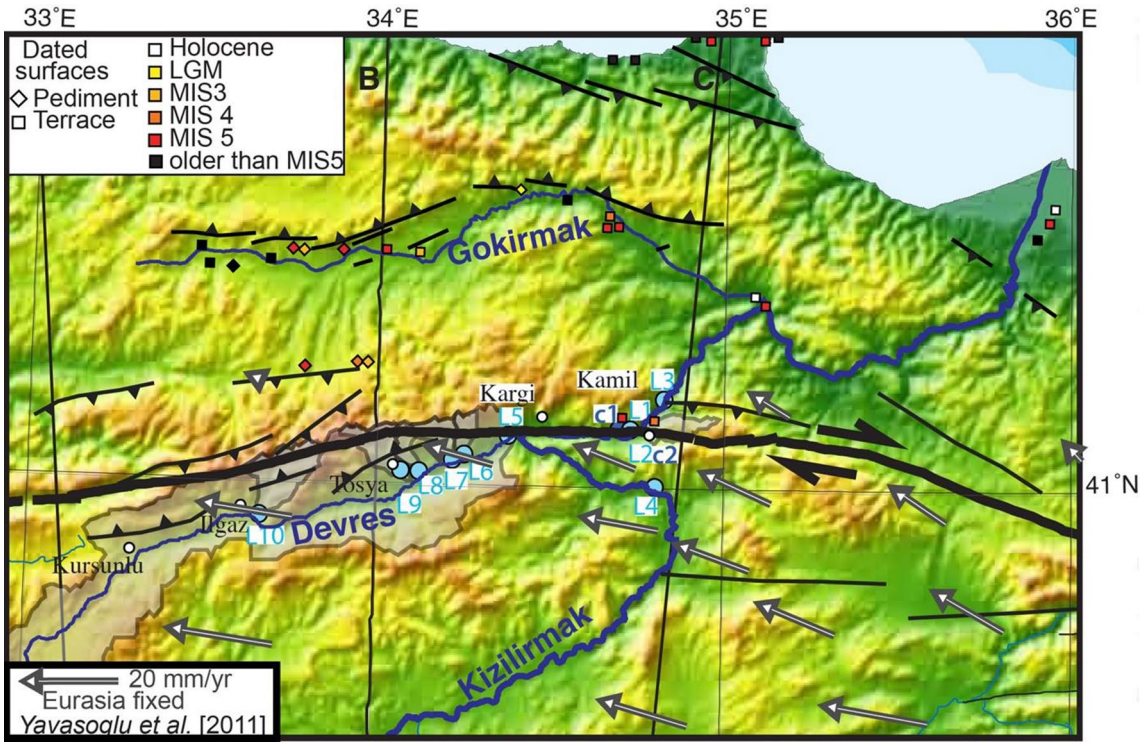

Fig. 9 The convex NAF central arc forming an orogenic wedge associated with thrust faulting. GPS vectors from Yavaşoğlu et al. (2011) outlined the expected convergence in the region of Kargı, Kamil, Tosya and Ilgaz cities. Dated ulipfted surfaces are indicated with colors according to their exposure ages [north of the Kızılırmak, work of Yıldırım et al. (2013a,b) and Berndt et al. (2018)]. Location of sand samples for erosion rates are indicated with blue circles, the catchment of the Devrez River is outlined in gray

(McClain et al. 2020) (Fig. 1a). **T3** in Kamil, thus, results from regional episode of strath planation that took place during MIS 5a/b. The **T3** formation occurred at the end of the Karangatian highstand in the Black Sea (Krijgsman et al. 2019) and is broadly coincident with the abrupt replacement of mixed forest by steppe species in the eastern Mediterranean area during MIS 5a (Litt et al. 2014). The vegetation and climatic changes are likely to have increased the sediment supply in the CP, as evidenced by the high erosion rates obtained from the Kızılırmak paleochannels. High sediment supply would have led to the strath planation in Kamil and more to the north or to the west in the Gökırmak and Filyos catchment, respectively. This climate-induced increase in sediment supply triggered a river aggradation episode. This episod is broadly recorded in the whole Mediterranean area and took place around 88 ka according to Macklin et al. (2002). It has been related to accelerated catchment erosion and lacustrine sedimentation (Allen et al. 1999; Fuller et al. 1998; Macklin et al. 2002). The subsequent river incision and terrace abandonment may be related to the base-level drop induced by the Black Sea Atelian regression that peaked at an age of 85-75 ka (Krijgsman et al. 2019). Terrace incision also occurred during this period along the Danube River [T4 cutting at 83 ± 11 kyr according to Armaş et al. (2019)].

The 67 ± 7 ka age of **T2** strath also corresponds to the ages of other strath terrace (i.e., 68 ± 6 ka, ^{36}Cl age) and pediments (60 ± 5 ka ^{10}Be age; 70 ± 7 ka ^{21}Ne age) in the Gökırmak catchment (Yıldırım et al. 2013a) (Fig. 9). Downstream along the Kızılırmak River gorge and the delta plain, lower fill terraces have 77.3 ± 5.6 ka, 71.2 ± 4.4 ka, 59.3 ± 6.2 ka OSL ages (Berndt et al. 2018). To the east, the age of a strath terrace along the Yeşilırmak River is similar (72.9 ± 4.4 ka) (Erturaç and Kıyak 2017). This planation is older than the youngest strath terrace formation in the Filyos Basin at 50.9 ± 2.8 ka (McClain et al. 2020) (Fig. 1a), but it corresponds also to a ~ 60 ka alluvial optima documented in the Duzce Basin (Pucci et al. 2008). **T2** would, thus, result from another regional episode of planation level that occurred during MIS4 (60–75 ka). This time period corresponds to a Black Sea lowstand (Panin and Popescu 2007). It is coeval with a large climate degradation that was recorded in the Sofular Cave located 100 km west of our study area (Fleitmann et al. 2009) and in the Lake Van record in eastern Turkey. There, the pollen record evidences the nearly complete disappearance of arboreal pollen (Pinius and Quercus) (Litt et al. 2014; Pickarski et al. 2015), which was synchronous with the second largest decrease in lake water level during the last 90 ka (Çağatay et al. 2014) and with the emplacement of lowstand deltas (Cukur et al. 2014). Changes in vegetation and in catchment hydrology, which are the primary control of sedimentation, may have triggered this second episode of strath planation in the Kamil Basin.

The strath terraces in the Kamil Basin are, thus, a response to climatic fluctuations like at other upstream and downstream locations along the Kızılırmak River (i.e., Yıldırım et al. 2013a; Doğan 2011; Çiner et al. 2015). Other river terraces in Turkey (Westaways et al. 2004), in the Mediterranean area (Bridgland, 2000; Macklin et al. 2002) have also systematically been attributed to climate forcing.

In Kamil, **T1** attest for a large fluvial aggradation (Fraser et al. 2010a). The ~ 25 m thick **T1** aggradational fill corresponds to a large sediment delivery (Fig. 2d). About 30 km more to the west, in the Kargı Basin, a fill terrace standing 30 m above the floodplain also exists. Our cosmogenic dating provides inconclusive ages (Tables S2 and S3). After MIS4, there were two distinct episodes of terrace formation along Turkish Rivers flowing to the Black Sea. The first one occurred during MIS3, around ~ 30–40 ka, and is attested along the Yeşilırmak River (48.5 ± 5 ka; 35 ± 3 ka) (Erturaç and Kıyak 2017), the Sakarya River (41 ± 2 ka; 30 ± 0.2 ka) (Erturaç et al. 2019), and downstream near the mouth of the Kızılırmak River (37 ± 3 ka; 32 ± 2 ka; 42 ± 4 ka). At that time, the high Black Sea level, the Surozhian highstand, is likely to have favored river aggradation. The second episode of aggradation occurred 18–15 kyr ago, along the Yeslislirmak River (18.5 ± 2.1 ka) (Erturaç and Kıyak 2017) and along the Kızılırmak floodplain downstream near its mouth (14 ± 3 ka; 14.9 ± 3 ka; 18.9 ± 7 ka) (Erturaç et al. 2019) and upstream in the Anatolian Plateau (16.5 cal ka) (Doğan 2011). According to Doğan (2011), this aggradation episode occurred after a main downcutting phase of the river, which started after later stages of MIS5 or early MIS4. The downcutting to aggradation change occurred during a pronounced climate change, the last glacial–interglacial transition (Langgut et al. 2011). The LGM to Holocene transition in Turkey is characterized by drastic vegetation (e.g., Valsecchi et al. 2012), precipitation (Jones et al. 2007) and temperature changes (Göktürk et al. 2011). The LGM has specific characteristics in Anatolia. First, evapotranspiration ratio was low, so there was a positive water balance with high lake levels in Anatolian (Roberts et al. 2011; Jones et al. 2007). Second, high snowfall and restricted vegetation cover were resulting in strong river discharge. Doğan (2010) inferred that these two factors leaded to a high discharge/sediment supply ratio during the glacial period in Turkey resulting in valley downcutting. The change during the Holocene transition to a more negative hydraulic balance resulted in a shift from downcutting to aggradational filling along the Kızılırmak as evidenced in the Central Anatolian Plateau. Pucci et al. (2008) also documented this alluviation phase at the transition from arid to humid conditions in the Duzce Basin. Finally, the period also corresponds to a Black Sea hightstand linked to a high input in glacier meltwater increasing the Black Sea level (Panin and Popuesco 2007), which triggered its overflowing to the Marmara Sea (Çağatay et al.

2016). Regarding **T1**, it is not possible to decipher to which period aggradation period, MIS3 (~ 30–40 ka) or LGM, it is related without more dating constraints.

6.2 Geological strike-slip motion along the NAF

T3 provides some constrains on the NAF quaternary slip rate. No other slip rate estimates exist in the central NAF over the 20–100 ka time frame (Şengör and Zabcı 2019, 2019). We documented a 715–845 m long offset of **T3** eastern margin and a 310 m offset of the Koz stream. The incision of the Koz stream has separated the **eastern** and **western T3** surfaces and is inferred to be much younger than **T3** age. On **T3W** cosmogenic dating indicates that most marbles cobbles were emplaced at 21 ± 2 ka during the LGM (Fig. 6). Koz incision that impedes the emplacement of these cobbles on the T3E surface must be older. We obtain in that way a maximum slip rate of 14.8 mm/year. Similarly, the larger **T3** offset started after the incision and abandonment of **T3** at 83 ± 15 ka. This offset constrains the geological slip rate on the NAF over this time frame to be around 10 mm/year.

The obtained slip rates are lower than the Holocene slip nearby (Hubert-Ferrari et al. 2000; Kozacı et al. 2007; Kozacı et al. 2009) (see Sect. 2.1), the geodetic rate inferred using a local network measured (17–22 mm/year) (Yavaşoğlu et al. 2011) and using Insar velocity profiles (21 mm/year, average with 14–29 mm/year 95%CI in Hussain et al. (2016), 23 mm/year average with 17–31 mm/year 95% CI in Hussain et al (2018)). It is also lower than the longer-term 15 mm/year geological slip rate obtained considering that the Kızılırmak established its course across the CP ~ 2 Ma (Hubert-Ferrari et al. 2000; Yıldırım et al. 2011) and its 30 km long offset between the Kamil and the Kargı pull-apart. Considering the review of Zabcı (2019) about NAF geological and geodetic and slip rates, the obtained rate is among the lowest estimates.

These low geological rates can be linked to different factors. First, the **T3** margins are irregular, are offset near **T3** southern tip, and they may have undergone lateral strong erosion . So, our measurements are not highly accurate. For the Koz stream we also have no direct dating of its incision. Second, even if most deformation takes places on the NAF offsetting **T3**, a part can be accommodated on a relatively broad zone around (Barka and Hancock 1984) called the North Anatolian Shear Zone (e.g., Şengör et al. 2005; Şengör and Zabcı 2019). Indeed, the geology in the CP is composed of a serie of amalgamated terrains separated by various inactive E–W fault structures that are optimally oriented in the present-day stress field to accommodate some deformation. In that case, Vallage et al. (2016) have shown that geologic structures can accommodate a significant part of the deformation in a band associated with the main long-term fault plane. This process was also considered along the NAF to reconcile geodetic and 2–12 ka rates by Zabcı (2019). However, the difference between our geological rates and the other geological rates obtained over 2–12 ka would imply that the slip partitioning between the NAF and these structures changes through times as observed on other faults (e.g., Bennet et al. 2004; Ninis et al. 2013). Third, the short-term data may also not be fully representative of the longer geological time-scale deformations. Gasperini et al. (2011) obtained in the Marmara region a NAF geological slip rate that is about one half of the one expected from plate motion (Polonia et al. 2004), and Zabcı (2019) evidenced long-term slip change in Cinarcik Basin. This is also the case for the Karakorum strike-slip faut whose geological rate is ten times larger than its geodetic rate (Chevalier et al. 2005). Similarly, the Garlock Fault in California shows no present-day accumulating deformation, but it has a ~ 5 mm/year geological slip rate (Peltzer et al. 2011). This case can be related to the mechanical properties of the lithosphere (Zabcı 2019) or to change in stress pattern in relation with spatiotemporal patterns of deformation within the Arabian-Eurasian collision zone. The spatio-temporal interaction between the NAF and the EAF have already been evidenced Hubert-Ferrari et al. (2003) and Fraser et al. (2010) and suggested that time-varying fault-normal stress in relation with different patterns of deformation along the Anatolian plate boundaries influence the seismic cycle of the NAF. Along the NAF, more long-term slip estimates are needed to pin-point the mechanisms at play.

6.3 Uplift gradient in the Central Pontides

T3 and **T2** also provide information on the river incision rate and rock uplift over the last 130 ka in the CP. Given the height and age of the terraces, an identical incision rate of 1 mm/year is inferred for both terraces. The obtained incision rate based on two terrace remnants is integrated over a glacial/interglacial cycle and can thus be applied as a proxy for uplift following Hancock and Anderson (2002) or Wegmann and Pazzaglia (2002). In the Gökırmak watershed located just north of the Kamil Basin, river incision rates were similarly inferred to represent uplift rates (Fig. 9) (Yıldırım et al. 2013a).

Our rate can be compared to the 0.28 mm/year rate (Yıldırım et al. 2013a) derived in the Gökırmak catchment located 40 km to the northeast and at the mouth of the Kızılırmak River near the Black Sea coast (Berndt et al. 2018) because they are not separated by a knickpoint (Fig. 9). The fluvial incision rate at Kamil by the Kızılırmak River is three times higher than the fluvial incision rate in the Gökırmak catchment. The uplift rate close to the NAF is, thus, three times higher than in the Sinop Range or along the Black Sea coast to the north. This conclusion is in agreement with the CP topography as investigated by Yıldırım et al.

(2011) and illustrated in the present paper by topographic sections (Fig. 1). The CP close to the NAF shows higher fluvial base levels, higher ridge levels and higher relief compare to the Sinop range to the north.

The larger incision rate at the study location is also in agreement with the proposed tectonic model of the area. The CP are interpreted as a positive flower structure related to the convex bend of the NAF that is too narrow to accommodate without off-fault deformation the rotation of the Anatolian Plate. According to Yıldırım et al. (2013a), the related shortening is accommodated in a wide orogenic wedge, which reaches the Black Sea Coast and is responsible for the uplift of the CP. We evidence a non-uniform uplift within the CP Wedge with higher rate close to the NAF. It implies that the transpressional deformation is not accommodated evenly within the wedge. Therefore, even regarding shortening in the orogenic wedge, the NAF is still the main structure in the deformation pattern.

6.4 Erosion rates, cumulated shortening and the role of the NAF

The 395 mm/ka average erosion rate from the CP Rivers ranging is significantly higher than the 40 mm/ka erosion rate of the Central Anatolian Plateau (Aydar et al. 2013). We compared them to the present-day sediment discharge (solid phase) of some of the largest rivers in Turkey draining from the Anatolian Plateau to the Black Sea coast. The Sakarya, Kızılırmak and Yesilirmak Rivers are transporting, respectively, 8.8 Mt/year, 23 Mt/year, and 19 Mt/year as bedload (Meybeck et Ragu 1995). Given their respective drainage area and an average density of 2.7, an average erosion rate of 120 mm/ka can, thus, be obtained. The present-day average discharge at the river outlets is, thus, compatible with the longer-term denudation rates characterizing the Anatolian Plateau and the higher ones across the CP.

The basin average erosion rates are at least two times lower than the 1 mm/year incision rate of the Kızılırmak River. As a result, the Kızılırmak and Devrez Rivers form marked V-shaped valleys across the CP with a relief reaching over 1500 m (Fig. 1).

We use erosion rates and relief to retrieve a first-order mass balance of the CP (Fig. 10a). We evaluate a first-order cumulated shortening in the CP using the relief formed above a fixed reference (i.e., the theoretical topography in the region without deformation). Our reference level is the Kızılırmak base level because of its very low incision rate across the Central Anatolian Plateau (i.e., 50 mm/ka) (Çiner et al. 2015) and the low erosion rate of the plateau itself (i.e., 40 mm/ka) (Aydar et al. 2013). Farther north, it is also an adequate reference if we consider a steady-state equilibrium of the landscape with an incision rate equal to the uplift rate; its geometry is similar to the strait extension of the Kızılırmak base level from the Anatolian Plateau to the Black Sea coast.

On profiles A and B in Fig. 1 across the CP, the minimal uplifted area lies in between the lowest topographic level and the reference level (Figs. 1, 10b). Considering (1) an isostatic equilibrium, (2) a width of the range of about 200 km, (3) a crust of 30–40 km (Makris and Stobbe 1984; Vanacore et al. 2013), and (4) density of 2.8 and 3.3 for the crust and the mantle, we obtain a minimal shortening of 12–16 km. Considering a minimal erosion rate of about 120 mm/ka, we would need to add a shortening of 1.2 km over the last 2 Ma, and 3 km over the last 5 Ma.

This shortening rate is compared to the long-term shortening induced by the NAF geometry in its central convex bend over its history (Fig. 10c). Considering a cumulated lateral motion of the Anatolian Block of about 85 km (e.g., Hubert-Ferrari et al. 2002) along the small circle that best approximates the NAF trace from Erzincan in the East to the Marmara Sea in the west (Fig. 1), we obtain a 9 km cumulated shortening in its central part. This inferred shortening is significantly lower than the minimal shortening inferred in the CP. A first reason is that the NAF is not the only driver of the shortening. Part of the stress related to the Arabia-Eurasion collision may be transmitted across Anatolia to the north, and concentrated at the border with the more rigid oceanic lithosphere of the Black Sea. This would explain the large relief formed by the CP continuously along the whole southern Black Sea coast and the higher elevations more to east toward the Lesser Caucasus. A second possibility is that part of the shortening is inherited and might be linked to the westward NAF propagation process. In the central bend area, the NAF encounters a large number of former active faults, as the CP has a rich tectonic history and represents an amalgamation of various terrains since the Jurassic. Because of the large number of E-W trending tectonic pre-existing structures, a distributed deformation prior to the NAF emplacement as a main structure all the way to the surface, is likely to have taken place. This process was already inferred in Hubert-Ferrari et al. (2002) and was documented father west in the Marmara Sea (Karakaş et al. 2018).

7 Conclusion

Geomorphic mapping, ^{14}C dating and measurements of cosmogenic nuclide concentration in riverbeds and in cobbles on strath terraces constrain the deformation pattern of the central transpressive arc of the NAF over different scales.

- In the Kamil Basin, **T0,** the most recent fill terrace, was offset by ~ 14 ± 2 m during the last two major 1943 and 1668 earthquakes, which implies that the displacement per event along the 1943 segment is variable between

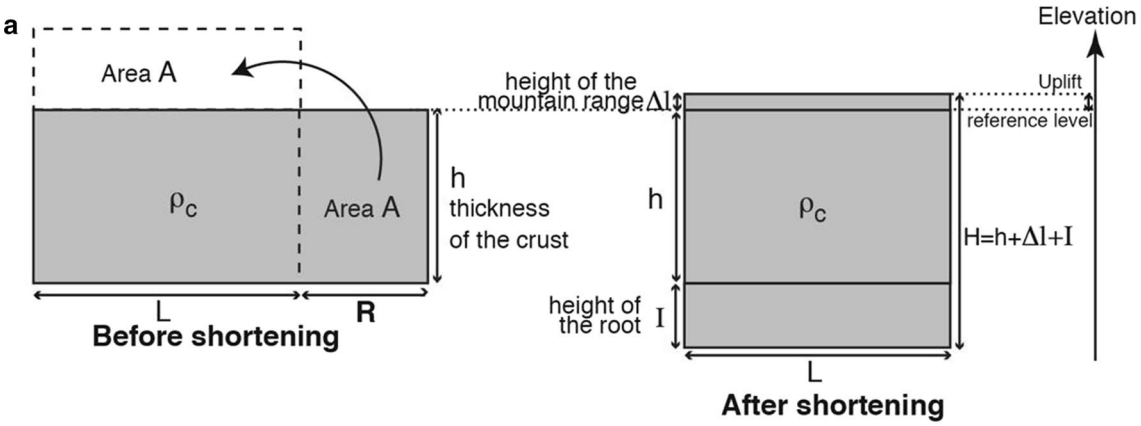

Mass conservation for incompressible rocks $(L+R)\ h = L\ (H+e)$ with e : height of the surface eroded

Isostatic equilibrium $\rho_c\ (h+I+\Delta l) = \rho_c\ h + \rho_m\ I$ with ρ_c=2.8 density of the crust, ρ_m=3.3 density of the mantel

Shortening $R = \frac{L\,\Delta l}{h}\,\frac{\rho_m}{\rho_m - \rho_c} + \frac{e\,L}{h}$

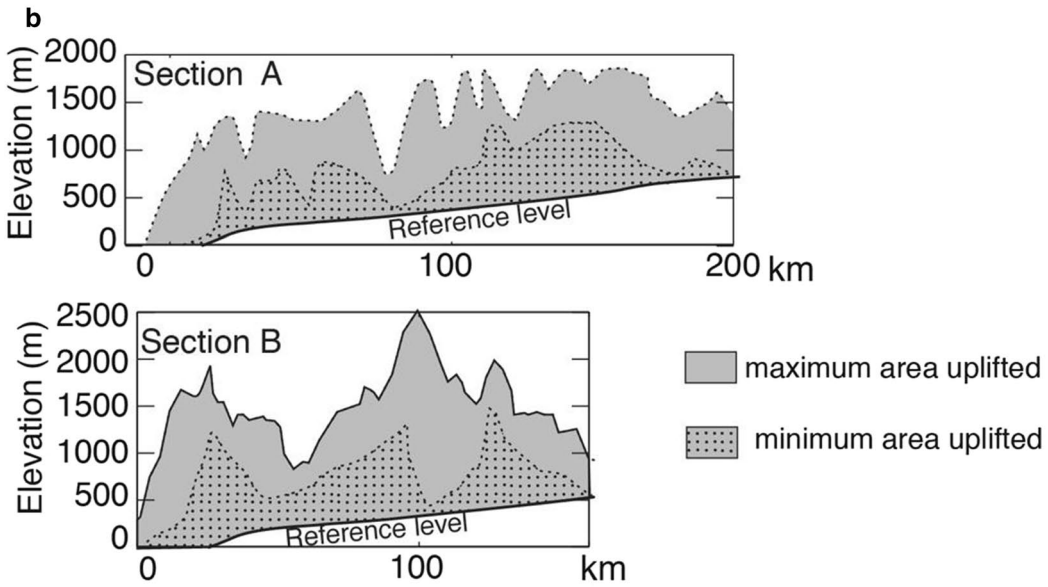

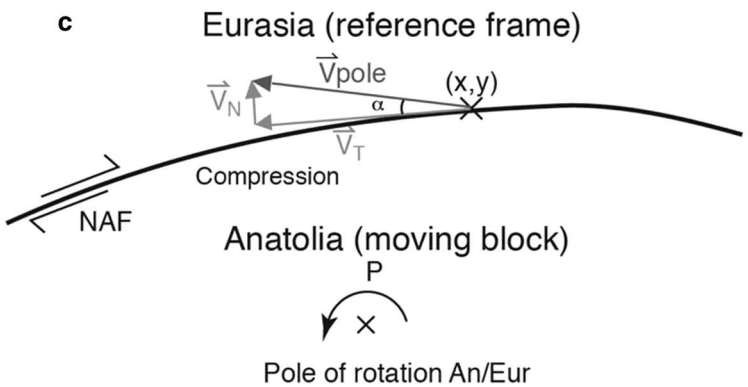

◂**Fig. 10** First-order shortening in the CP. **a** Mass balance considering isostasy, erosion and a cumulated shortening R. **b** Minimal and maximal uplifted surfaces along profiles A and B with respect to the reference level (Fig. 1). Once the surfaces are evaluated, shortening can be computed. **c** Shortening derived from the geometry of the NAF that is different from the small circle of the rotation pole of Anatolia/Eurasian or from GPS vectors forming an angle with respect to the NAF central bend. A cumulated Anatolian motion of 85 km would imply a 9 km shortening in the NAF central bend, if the Anatolia/Eurasia kinematics and NAF geometry stayed constant

seismic cycles, a pattern opposite to the 1944 segment (Kondo et al. 2010).

- A larger 715–845 m offset of the strath terrace **T3** was evidenced, which suggests a geological slip rate of 10 mm/year over the last 83 ka much lower than other geological rates (Zabcı 2019). It cannot be directly compared to other slip rates because it occurs on longer time scale. Possible explanations are (i) variable slip partitioning between the NAF and the numerous inherited E–W trending structures of the CP or (ii) slip changes in relation to mechanical properties of the lithosphere or spatio-temporal changes in deformation in the Arabian-Eurasian collision zone.

- **T3** and **T2** strath terraces have respective exposure ages of 83 ± 15 ka and 67 ± 7 ka. **T3** corresponds to a major Mediterranean river aggradation associated a high denudation rate in the mountains, the end of the Black Sea Karangatian highstand and the beginning of the Atelian regression (Krijgsman et al. 2019). **T2** strath planation correspond to a regional episode recorded along the northern part of the Kızılırmak and Yeşilırmak Rivers (Yıldırım et al. 2013a; Erturaç and Kıyak 2017; Berndt et al. 2018). **T3** and **T2** stand 95 and 75 m above the Kızılırmak floodplain, respectively, and their incision provided constraints regarding uplift in the CP. The resulting 1 mm/year uplift rate is higher than the 0.28 mm/year just to the north (Yıldırım et al. 2013a; Berndt et al. 2018). Transpressive deformation in the central orogenic wedge is, thus, not accommodated uniformly and is higher at the center of the flower structure formed by the NAF.

- We evidenced (1) a 160 m/Ma minimum denudation rate of the Kızılırmak catchment in the CP, which is three times higher than in the Central Anatolian Plateau, and (2) higher cosmogenic nuclide denudation rates in catchments directly affected by thrust faulting. Both results suggest a strong tectonic control of erosion rates in the CP and broadly in Anatolia.

- Finally, erosion rates and relief above the Kızılırmak base level were combined to infer a minimal shortening rate of 15–19 km in the CP. It is significantly larger than the local cumulated shortening induced by the NAF restraining geometry in its central part. We, thus, infer that the origin of the present-day relief in the CP is partly related to compressive stresses linked to the Arabian–Eurasian collision that are transmitted through the Anatolian Plateau and concentrated on amalgamated faulted terrains lying against the more homogeneous Black Sea oceanic lithosphere.

Key Points

- 1 mm/year uplift along the central transpressive segment of the North Anatolian Fault constrained by 83 and 67ka strath terraces
- Geological slip rate of about 10 mm/year over 85 ka lower than Holocene rates
- 83 ka strath planation along the Kızılırmak River corresponds to a major Mediterranean river aggradation event, high denudation rates in the Central Pontides mountains and a highstand-lowstand transition in the Black Sea
- Variable displacement per event along the central segment of the North Anatolian Fault that last ruptured in 1943 and 1668
- Holocene cosmogenic-based denudation rates in the Central Pontides are high and mostly controlled by tectonics
- Cumulated deformation in the Central Pontides Range is only partly controlled and induced by the North Anatolia Fault
- Cobbles bought by frost-cracking, a dominant mechanism during Glacial Periods, cover the alluvial terraces

Supplementary Information The online version contains supplementary material available at https://doi.org/10.1007/s42990-021-00057-6.

Acknowledgements Our field study was greatly enhanced by the organizing assistance of Erhan Altunnel from Osmangazi University, Eskishir, Turkey. The trenches were opened by Jeff Fraser. Many thanks to Sevgi Altinok and Cagil Karakas for help in the field. We acknowledge the European Commission for funding this project as part of the Marie Curie Excellence Grant Project "Understanding the Irregularity of Seismic Cycles: A Case Study in Turkey" (MEXT-CT-2005-025617: Seismic Cycles). We are thankful to an anonymous reviewer as well as to Cengiz Zabcı that significantly contributes to improving the paper by his detailed review. Supplemental information and data would be found below.

References

Akçar N, Yavuz V, Ivy-Ochs S, Reber R, Kubik PW, Zahno C, Schlüchter C (2014) Glacier response to the change in atmospheric circulation in the eastern Mediterranean during the Last Glacial Maximum. Quat Geochronol 19:27–41

Aktuğ B, Doğru A, Özener H, Peyret M (2015) Slip rates and locking depth variation along central and easternmost segments of North Anatolian Fault. Geophys J Int 202(3):2133–2149

Allen JR, Brandt U, Brauer A, Hubberten HW, Huntley B, Keller J, Kraml M, Mackensen A, Mingram J, Negendank, Nowaczyk NR, Oberhansli H, Watts WA, Wulf S, Zolitschka B (1999) Rapid environmental changes in southern Europe during the last glacial period. Nature 400(6746):740

Allmendinger RW, Reilinger R, Loveless J (2007) Strain and rotation rate from GPS in Tibet, Anatolia, and the Altiplano. Tectonics 26:TC3013. https://doi.org/10.1029/2006TC002030

Ambraseys NN (1970) Some characteristic features of the Anatolian fault zone. Tectonophysics 9(2–3):143–165

Ambraseys NN, Finkel CF (1988) The Anatolian earthquake of 17 August 1668. In Symposium on historical seismograms and earthquakes (pp 173–180)

Anderson RS, Anderson SP (2010) Geomorphology: the mechanics and chemistry of landscapes. Xvi+637pp. Cambridge University Press (**ISBN 978 0 521 51978 6**)

Anderson RS, Anderson SP, Tucker GE (2013) Rock damage and regolith transport by frost: an example of climate modulation of the geomorphology of the critical zone. Earth Surf Proc Land 38(3):299–316

Andrieux J, Över S, Poisson A, Bellier O (1995) The North Anatolian Fault Zone: distributed Neogene deformation in its northward convex part. Tectonophysics 243(1–2):135–154

Applegate PJ, Urban NM, Keller K, Lowell TV, Laabs BJ, Kelly MA, Alley RB (2012) Improved moraine age interpretations through explicit matching of geomorphic process models to cosmogenic nuclide measurements from single landforms. Quatern Res 77(2):293–304

Armijo R, Lyon-Caen H, Papanastassiou D (1992) East-west extension and Holocene normal-fault scarps in the Hellenic arc. Geology 20(6):491–494

Armaş I, Necea D, Miclăuş C (2019) Fluvial terrace formation and controls in the Lower River Danube, SE Romania. Quatern Int 504:5–23

Armitage JJ, Duller RA, Whittaker AC, Allen PA (2011) Transformation of tectonic and climatic signals from source to sedimentary archive. Nat Geosci 4(4):231

Arnold M et al (2010) The French accelerator mass spectrometry facility ASTER: improved performance and developments. Nuclear Instrum Methods Phys Res Sect B 268(11–12):1954–1959

Aydar E, Cubukcu HE, Şen E, Akın L (2013) Central Anatolian Plateau, Turkey: incision and paleoaltimetry recorded from volcanic rocks. Turkish J Earth Sci 22:739–746

Badertscher S, Fleitmann D, Cheng H, Edwards RL, Göktürk OM, Zumbühl A et al (2011) Pleistocene water intrusions from the Mediterranean and Caspian seas into the Black Sea. Nat Geosci 4(4):236

Balco G, Stone JO, Lifton NA, Dunai TJ (2008) A complete and easily accessible means of calculating surface exposure ages or erosion rates from 10Be and 26Al measurements. Quat Geochronol 3(3):174–195

Ballato P, Parra M, Schildgen TF, Dunkl I, Yıldırım C, Özsayın E et al (2018) Multiple exhumation phases in the Central Pontides (N Turkey): new temporal constraints on major geodynamic changes associated with the closure of the Neo-Tethys Ocean. Tectonics 37(6):1831–1857

Barka AA (1984) Geology and tectonic evolution of some Neogene-Quaternary basins in the North Anatolian fault zone, special publication. Geol Soc Turk 209–227

Barka A (1996) Slip distribution along the North Anatolian fault associated with the large earthquakes of the period 1939 to 1967. Bull Seismol Soc Am 86(5):1238–1254

Barka AA, Hancock PL (1984) Neotectonic deformation patterns in the convex-northwards arc of the North Anatolian fault zone. Geol Soc Lond Special Public 17(1):763–774

Barka AA, Kadinsky-Cade K (1988) Strike-slip fault geometry in Turkey and its influence on earthquake activity. Tectonics 7(3):663–684

Benedetti L, Finkel R, Papanastassiou D, King G, Armijo R, Ryerson F et al (2002) Post-glacial slip history of the Sparta fault (Greece) determined by 36Cl cosmogenic dating: evidence for non-periodic earthquakes. Geophys Res Lett 29(8):87–91

Berndt C, Yıldırım C, Çiner A, Strecker MR, Ertunç G, Sarıkaya MA et al (2018) Quaternary uplift of the northern margin of the Central Anatolian Plateau: new OSL dates of fluvial and delta-terrace deposits of the Kızılırmak River, Black Sea coast, Turkey. Quatern Sci Rev 201:446–469

Bierman P, Steig EJ (1996) Estimating rates of denudation using cosmogenic isotope abundances in sediment. Earth Surf Proc Land 21(2):125–139

Borchers B, Marrero S, Balco G, Caffee M, Goehring B, Lifton N et al (2016) Geological calibration of spallation production rates in the CRONUS-Earth project. Quat Geochronol 31:188–198

Bridgland DR (2000) River terrace systems in north-west Europe: an archive of environmental change, uplift and early human occupation. Quatern Sci Rev 19(13):1293–1303

Brown ET, Bourlès DL, Colin F, Raisbeck GM, Yiou F, Desgarceaux S (1995) Evidence for muon-induced production of 10Be in near-surface rocks from the Congo. Geophys Res Lett 22(6):703–706

Brown ET, Molnar P, Bourlés DL (2005) Comment on "Slip-rate measurements on the 630 Karakorum Fault may imply secular variations in fault motion." Science 309:1326b

Burbank DW, Anderson RS (2009) Tectonic geomorphology. Wiley

Çağatay MN, Öğretmen N, Damcı E, Stockhecke M, Sancar Ü, Eriş KK, Özeren S (2014) Lake level and climate records of the last 90 ka from the Northern Basin of Lake Van, eastern Turkey. Quatern Sci Rev 104:97–116

Çağatay MN, Alpar B, Kirci Elmas E, Caner H, Vardar D (2016) Late quaternary paleoceanographic and paloclimatic evolution of the sea of marmara. In: Özsoy E, Balkis N, Balkis N (eds) The sea of marmara, marine biodiversity, fisheries, conservation and governance. Turkish Marine Research Foundation Publication No: 42, Istanbul, 256–281

Cavalié O, Jónsson S (2014) Block-like plate movements in eastern Anatolia observed by InSAR. Geophys Res Lett 41(1):26–31

Cavazza C, Federici I, Okay AI, Zattin M (2012) Apatite fissiontrack thermochronology of the Western Pontides (NW Turkey). Geol Mag 149:133–140

Chevalier ML, Ryerson FJ, Tapponnier P, Finkel RC, Van Der Woerd J, Haibing L, Qing L (2005) Slip-rate measurements on the Karakorum fault may imply secular variations in fault motion. Science 307(5708):411–414

Chmeleff J, von Blanckenburg F, Kossert K, Jakob J (2010) Determination of the 10Be half-life by multicollector ICP-MS and liquid scintillation counting. Nucl Inst Methods Phys Res B 268:192–199

Chuang RY, Johnson KM (2011) Reconciling geologic and geodetic model fault slip-rate discrepancies in Southern California: consideration of nonsteady mantle flow and lower crustal fault creep. Geology 39(7):627–630

Çiner A, Doğan U, Yıldırım C, Akçar N, Ivy-Ochs S, Alfimov V et al (2015) Quaternary uplift rates of the Central Anatolian Plateau, Turkey: insights from cosmogenic isochron-burial nuclide dating of the Kızılırmak River terraces. Quatern Sci Rev 107:81–97

Çinku MC, Hisarlı ZM, Heller F, Orbay N, Ustaömer T (2011) Middle Eocene paleomagnetic data from the eastern Sakarya Zone and the central Pontides: implications for the tectonic evolution of north central Anatolia. Tectonics. https://doi.org/10.1029/2010TC002705

Cukur D, Krastel S, Schmincke HU, Sumita M, Çağatay MN, Meydan AF et al (2014) Seismic stratigraphy of lake Van, eastern Turkey. Quatern Sci Rev 104:63–84

Daout S, Barbot S, Peltzer G, Doin M-P, Liu Z, Jolivet R (2016) Constraining the kinematics of metropolitan Los Angeles faultswith a slip-partitioning model. Geophys Res Lett 43:11192–11201. https://doi.org/10.1002/2016GL071061

D'Arcy M, Roda-Boluda DC, Whittaker AC (2017) Glacial-interglacial climate changes recorded by debris flow fan deposits, Owens Valley, California. Quatern Sci Rev 169:288–311

Desilets D, Zreda M, Prabu T (2006) Extended scaling factors for in situ cosmogenic nuclides: new measurements at low latitude. Earth Planet Sci Lett 246(3–4):265–276

Doğan U (2010) Fluvial response to climate change during and after the Last Glacial Maximum in Central Anatolia. Turkey Quater Int 222(1–2):221–229

Doğan U (2011) Climate-controlled river terrace formation in the Kızılırmak Valley, Cappadocia section, Turkey: inferred from Ar–Ar dating of Quaternary basalts and terraces stratigraphy. Geomorphology 126(1–2):66–81

Edmond JM, Huh Y (1997) Chemical weathering yields from basement and orogenic terrains in hot and cold climates. In Tectonic uplift and climate change. Springer, Boston, pp 329–351

Erturaç MK, Kıyak N (2017) Investigating the fluvial response to late pleistocene climate changes and vertical deformation: Yeşilırmak Terrace Staircases (central north Anatolia). Geol Bull Turkey 60:615–636

Erturaç MK, Şahiner E, Zabcı C, Okur H, Polymeris GS, Meriç N, İkiel C (2019) Fluvial response to rising levels of the Black Sea and to climate changes during the Holocene: luminescence geochronology of the Sakarya terraces. The Holocene 29(6):941–952

Farber DL, Mériaux AS, Finkel RC (2008) Attenuation length for fast nucleon production of 10Be derived from near-surface production profiles. Earth Planet Sci Lett 274(3–4):295–300

Fleitmann D, Cheng H, Badertscher S, Edwards RL, Mudelsee M, Göktürk OM et al (2009) Timing and climatic impact of Greenland interstadials recorded in stalagmites from northern Turkey. Geophys Res Lett. https://doi.org/10.1029/2009GL040050

Fraser J, Hubert-Ferrari A, Vanneste K, Altinok S, Drab L (2010b) A relict paleoseismic record of seven earthquakes between 2000 BC and 600 AD on the central North Anatolian fault at Elmacik, near Osmancik, Turkey. Bulletin 122(11–12):1830–1845

Fraser J, Vanneste K, Hubert-Ferrari A (2010a) Recent behavior of the North Anatolian Fault: Insights from an integrated paleoseismological data set. J Geophys Res. https://doi.org/10.1029/2009JB006982

Fuller IC, Macklin MG, Lewin J, Passmore DG, Wintle AG (1998) River response to high-frequency climate oscillations in southern Europe over the past 200 kyear. Geology 26(3):275–278

Fuller TK, Perg LA, Willenbring JK, Lepper K (2009) Field evidence for climate-driven changes in sediment supply leading to strath terrace formation. Geology 37(5):467–470

Gasperini L, Polonia A, Çağatay MN, Bortoluzzi G, Ferrante V (2011) Geological slip rates along the North Anatolian Fault in the Marmara region. Tectonics. https://doi.org/10.1029/2011TC002906

Göktürk OM, Fleitmann D, Badertscher S, Cheng H, Edwards RL, Leuenberger M et al (2011) Climate on the southern Black Sea coast during the Holocene: implications from the Sofular Cave record. Quatern Sci Rev 30(19–20):2433–2445

Gosse JC, Phillips FM (2001) Terrestrial in situ cosmogenic nuclides: theory and application. Quatern Sci Rev 20(14):1475–1560

Granger DE, Smith AL (2000) Dating buried sediments using radioactive decay and muogenic production of 26Al and 10Be. Nucl Instrum Methods Phys Res Sect B 172(1–4):822–826

Granger DE, Kirchner JW, Finkel R (1996) Spatially averaged long-term erosion rates measured from in situ-produced cosmogenic nuclides in alluvial sediment. J Geol 104(3):249–257

Hales TC, Roering JJ (2007) Climatic controls on frost cracking and implications for the evolution of bedrock landscapes. J Geophys Res 112(F2). https://doi.org/10.1029/2006JF000616

Hancock GS, Anderson RS (2002) Numerical modeling of fluvial strath-terrace formation in response to oscillating climate. Geol Soc Am Bull 114(9):1131–1142

Herece E, Akay E (2003) Atlas of North Anatolian Fault (NAF)/ Kuzey Anadolu Fayi Atlasi (KAF). General directorate of mineral research and exploration, special publication series-2, Ankara, 61 p+13 appendices as separate maps. ISBN 975659554X.

Hetzel R, Niedermann S, Tao M, Kubik PW, Strecker MR (2006) Climatic versus tectonic control on river incision at the margin of NE Tibet: 10Be exposure dating of river terraces at the mountain front of the Qilian Shan. J Geophys Res 111(F3). https://doi.org/10.1029/2005JF000352

Hubert-Ferrari A, Armijo R, Meyer B, King GCP, Barka A (2002) Morphology, displacement and slip rates along the North Anatolian Fault (Turkey). J Geophys Res. https://doi.org/10.1029/2001JB000393

Hubert-Ferrari A, King G, Manighetti I, Armijo R, Meyer B, Tapponnier P (2003) Long-term elasticity in the continental lithosphere; modelling the Aden Ridge propagation and the Anatolian extrusion process. Geophys J Int 153(1):111–132

Hubert-Ferrari A, Avşar U, El Ouahabi M, Lepoint G, Martinez P, Fagel N (2012) Paleoseismic record obtained by coring a sag-pond along the North Anatolian Fault (Turkey). Ann Geophys 55(5):929–953

Hussain E, Hooper A, Wright TJ, Walters RJ, Bekaert DP (2016) Interseismic strain accumulation across the central North Anatolian Fault from iteratively unwrapped InSAR measurements. J Geophys Res 121(12):9000–9019

Hussain E, Wright TJ, Walters RJ, Bekaert DP, Lloyd R, Hooper A (2018) Constant strain accumulation rate between major earthquakes on the North Anatolian Fault. Nat Commun 9(1):1392

Jones MD, Roberts CN, Leng MJ (2007) Quantifying climatic change through the last glacial–interglacial transition based on lake isotope palaeohydrology from central Turkey. Quatern Res 67(3):463–473

Karakaş Ç, Armijo R, Lacassin R, Suc JP, Melinte-Dobrinescu MC (2018) Crustal strain in the Marmara pull-apart region associated with the propagation process of the North Anatolian Fault. Tectonics 37(5):1507–1523

Karasözen E, Özacar AA, Biryol CB, Beck SL (2013) Seismicity, focal mechanisms and active stress field around the central segment of the North Anatolian Fault in Turkey. Geophys J Int 196(1):405–421

Kohl CP, Nishiizumi K (1992) Chemical isolation of quartz for measurement of in-situ-produced cosmogenic nuclides. Geochim Cosmochim Acta 56(9):3583–3587

Kondo H, Özaksoy V, Yıldirim C (2010) Slip history of the 1944 Bolu Gerede earthquake rupture along the North Anatolian fault system: Implications for recurrence behavior of multisegment earthquakes. J Geophys Res 115(B4). https://doi.org/10.1029/2009JB006413

Korschinek G, Bergmaier A, Faestermann T, Gerstmann UC, Knie K, Rugel G, Wallner A, Dillmann I, Dollinger G, von Gostomski LC, Kossert K, Maitia M, Poutivtsev M, Remmert A (2010) A new value for the half-life of 10Be by heavy-ion elastic recoil detection and liquid scintillation counting. Nuclear Inst Methods Phys Res B. 268:187–191

Kozacı O, Dolan JF, Finkel RC, Hartleb RD (2007) Late Holocene slip rate for the North Anatolian Fault, Turkey, from cosmogenic

36Cl geochronology: implications for the constancy of fault loading and strain release rates. Geology 35:867–870. https://doi.org/10.1130/G23187A.1

Kozacı Ö, Dolan JF, Finkel RC (2009) A late Holocene slip rate for the central North Anatolian fault, at Tahtaköprü, Turkey, from cosmogenic 10Be geochronology: Implications for fault loading and strain release rates. J Geophys Res 114(B1). https://doi.org/10.1029/2008JB005760

Kozacı O, Dolan J, Yonlü O, Hartleb R (2011) Paleoseismologic evidence for the relatively regular recurrence of infrequent, large-magnitude earthquakes on the eastern North Anatolian Fault at Yaylabeli, Turkey. Lithosphere 3:37–54. https://doi.org/10.1130/L118.1

Kreemer C, Holt WE, Haines AJ (2003) An integrated global model of present-day plate motions and plate boundary deformation. Geophys J Int 154(1):8–34

Krijgsman W, Tesakov A, Yanina T, Lazarev S, Danukalova G, Van Baak CG et al (2019) Quaternary time scales for the Pontocaspian domain: Interbasinal connectivity and faunal evolution. Earth Sci Rev 188:1–40

Langgut D, Almogi-Labin A, Bar-Matthews M, Weinstein-Evron M (2011) Vegetation and climate changes in the South Eastern Mediterranean during the Last Glacial-Interglacial cycle (86 ka): new marine pollen record. Quatern Sci Rev 30(27–28):3960–3972

Le Dortz K, Meyer B, Sébrier M, Nazari H, Braucher R, Fattahi M et al (2009) Holocene right-slip rate determined by cosmogenic and OSL dating on the Anar fault, Central Iran. Geophys J Int 179(2):700–710

Lifton N, Sato T, Dunai TJ (2014) Scaling in situ cosmogenic nuclide production rates using analytical approximations to atmospheric cosmic-ray fluxes. Earth Planet Sci Lett 386:149–160

Litt T, Pickarski N, Heumann G, Stockhecke M, Tzedakis PC (2014) A 600,000 year long continental pollen record from Lake Van, eastern Anatolia (Turkey). Quatern Sci Rev 104:30–41

Macklin MG, Fuller IC, Lewin J, Maas GS, Passmore DG, Rose J et al (2002) Correlation of fluvial sequences in the Mediterranean basin over the last 200 ka and their relationship to climate change. Quatern Sci Rev 21(14–15):1633–1641

Makris J, Stobbe C (1984) Physical properties and state of the crust and upper mantle of the Eastern Mediterranean Sea deduced from geophysical data. Mar Geol 55(3–4):347–363

Martin LCP, Blard PH, Balco G, Lavé J, Delunel R, Lifton N, Laurent V (2017) The CREp program and the ICE-D production rate calibration database: a fully parameterizable and updated online tool to compute cosmic-ray exposure ages. Quat Geochronol 38:25–49

Matsuoka N (2008) Frost weathering and rockwall erosion in the southeastern Swiss Alps: long-term (1994–2006) observations. Geomorphology 99(1–4):353–368

McClain KP, Yıldırım C, Çiner A, Şahin S, Sarıkaya MA, Özcan O, Kıyak NG, Öztürk T (2020) Quaternary rock uplift rates and their implications for the western flank of the North Anatolian Fault restraining bend; inferences from fluvial terrace ages. Tectonics 39:e2019TC005993. https://doi.org/10.1029/2019TC005993

McKenzie D (1972) Active tectonics of the Mediterranean region. Geophys J Roy Astron Soc 30(2):109–185

Mériaux AS, Tapponnier P, Ryerson FJ, Xiwei X, King G, Van der Woerd J et al (2005) The Aksay segment of the northern Altyn Tagh fault: Tectonic geomorphology, landscape evolution, and Holocene slip rate. J Geophys Res 110(B4). https://doi.org/10.1029/2004JB003210

Meybeck M, Ragu A (1995) River discharges to the oceans: An assessment of suspended solids, major ions and nutrients. UN Environ. Programme, Nairobi, p 245

Morewood NC, Roberts GP (2000) The geometry, kinematics and rates of deformation within an en échelon normal fault segment boundary, central Italy. J Struct Geol 22(8):1027–1047

Mudd SM, Harel MA, Hurst MD, Grieve SW, Marrero SM (2016) The CAIRN method: automated, reproducible calculation of catchment-averaged denudation rates from cosmogenic nuclide concentrations. Earth Surf Dyn 4(3):655–674

Mudie PJ, Marret F, Aksu AE, Hiscott RN, Gillespie H (2007) Palynological evidence for climatic change, anthropogenic activity and outflow of Black Sea water during the last Pleistocene and Holocene: centennial- to decadal-scale records from the Black and Marmara Seas. Quatern Int 167–168:73–90

Nishiizumi K (2004) Preparation of 26Al AMS standards. Nucl Instrum Methods Phys Res, Sect B 223:388–392

Okay AI, Tüysüz O (1999) Tethyan sutures of northern Turkey. In: Durand B et al (eds) The Mediterranean Basins: tertiary extension within the Alpine Orogen, vol 156. Geological Society, London, pp 475–515 (**Special Publication, Oxford, UK**)

Okay AI, Sunal G, Sherlock S, Kylander-Clark AR, Özcan E (2020) İzmir-Ankara Suture as a Triassic to Cretaceous Plate Boundary—Data From Central Anatolia. Tectonics 39(5):e2019TC005849

Ottria G, Pandolfi L, Catanzariti R, Da Prato S, Ellero A, Frassi C et al (2017) Evolution of an early Eocene pull-apart basin in the Central Pontides (Northern Turkey): new insights into the origin of the North Anatolian Shear Zone. Terra Nova 29(6):392–400

Over S, Bellier O, Poisson A, Andrieux J, Tutkun Z (1993) Late Cenozoic fault kinematics within basins along the central North Anatolian fault zone (turkey). Comptes Rendus de l'Académie des Sciens Serie II 317(6):827–833

Panin N, Popescu I (2007) The northwestern Black Sea: climatic and sea-level changes in the Late Quaternary. In: The Black Sea flood question: changes in coastline, climate, and human settlement. Springer, Dordrecht, pp 387–404

Peltzer G, Crampé F, Hensley S, Rosen P (2001) Transient strain accumulation and fault interaction in the Eastern California shear zone. Geology 29(11):975–978

Peyret M, Masson F, Yavasoglu H, Ergintav S, Reilinger R (2013) Present-day strain distribution across a segment of the central bend of the North Anatolian Fault Zone from a Persistent-Scatterers InSAR analysis of the ERS and Envisat archives. Geophys J Int 192(3):929–945

Piccardi L, Gaudemer Y, Tapponnier P, Boccaletti M (1999) Active oblique extension in the central Apennines (Italy): evidence from the Fucino region. Geophys J Int 139(2):499–530

Pickarski N, Kwiecien O, Djamali M, Litt T (2015) Vegetation and environmental changes during the last interglacial in eastern Anatolia (Turkey): a new high-resolution pollen record from Lake Van. Palaeogeogr Palaeoclimatol Palaeoecol 435:145–158

Polonia A, Gasperini L, Amorosi A, Bonatti E, Bortoluzzi G, Cagatay N et al (2004) Holocene slip rate of the North Anatolian Fault beneath the Sea of Marmara. Earth Planet Sci Lett 227(3–4):411–426

Portenga EW, Bierman PR (2011) Understanding Earth's eroding surface with 10 Be. GSA Today 21(8):4–10

Pucci S, De Martini PM, Pantosti D (2008) Preliminary slip rate estimates for the Düzce segment of the North Anatolian Fault Zone from offset geomorphic markers. Geomorphology 97(3–4):538–554

Reber R, Akçar N, Yesilyurt S, Yavuz V, Tikhomirov D, Kubik PW, Schlüchter C (2014) Glacier advances in northeastern Turkey before and during the global Last Glacial Maximum. Quatern Sci Rev 101:177–192

Reilinger R, McClusky S, Vernant P, Lawrence S, Ergintav S, Cakmak R et al (2006) GPS constraints on continental deformation in

the Africa Arabia-Eurasia continental collision zone and implications for the dynamics of plate interactions. J Geophys Res 111(B5). https://doi.org/10.1029/2005JB004051

Roberts N, Reed JM, Leng MJ, Kuzucuoğlu C, Fontugne M, Bertaux J et al (2001) The tempo of Holocene climatic change in the eastern Mediterranean region: new high-resolution crater-lake sediment data from central Turkey. The Holocene 11(6):721–736

Schimmelpfennig I, Benedetti L, Finkel R, Pik R, Blard PH, Bourles D et al (2009) Sources of in-situ 36Cl in basaltic rocks. Implications for calibration of production rates. Quat Geochronol 4(6):441–461

Schimmelpfennig I, Benedetti L, Garreta V, Pik R, Blard PH, Burnard P et al (2011) Calibration of cosmogenic 36 Cl production rates from Ca and K spallation in lava flows from Mt. Etna (38 N, Italy) and Payun Matru (36 S, Argentina). Geochim Cosmochim Acta 75(10):2611–2632

Schumilovskikh LS, Fleitmann D, Nowaczyk NR, Behling H, Marret F, Wegwerth A, Arz HW (2014) Orbital and millenial-scale environmental changes between 64 and 25 ka BP recorded in Black Sea sediments. Climate of the Past 10:939–945

Şengör AMC, Yilmaz Y (1981) Tethyan evolution of Turkey: a plate tectonic approach. Tectonophysics 75(3–4):181–241

Şengör AC, Zabcı C (2019) The north Anatolian fault and the north Anatolian shear zone. In Landscapes and landforms of Turkey. Springer, Cham, pp 481–494

Şengör AMC, Tüysüz O, Imren C, Sakınç M, Eyidoğan H, Görür N et al (2005) The North Anatolian fault: A new look. Annu Rev Earth Planet Sci 33:37–112

Shumilovskikh LS, Tarasov P, Arz HW, Fleitmann D, Marret F, Nowaczyk N, Plessen B, Schlütz F, Behling H (2012) Vegetation and environmental dynamics in the southern Black Sea region since 18 kyr BP derived from the marine core 22-GC3. Palaeogeogr Palaeocl 337–338:177–193

Shumilvskikh LS, Arz H, Fleitmann D, Marret F, Nowaczyk N, Tarasov P, Wegwerth A, Behling H (2013) Vegetation and environmental changes in Northern Anatolia during penultimate deglaciation and Eemian recorded in Black Sea sediments. Quat Res 80:349–360

Siame LL, Angelier J, Chen RF, Godard V, Derrieux F, Bourlès DL et al (2011) Erosion rates in an active orogen (NE-Taiwan): a confrontation of cosmogenic measurements with river suspended loads. Quat Geochronol 6(2):246–260

Stone JO (2000) Air pressure and cosmogenic isotope production. J Geophys Res 105:23753–23759

Streig AR, Weldon RJ, Biasi G, Dawson TE, Gavin DG, Guilderson TP (2020) New insights into paleoseismic age models on the northern San Andreas Fault: charcoal inbuilt ages and updated earthquake correlations. Bull Seismol Soc Am 110(3):1077–1089

Sugai T, Awata Y, Anma R, Saka Y (1999) North Anatolian Fault in Turkey. J Geol Soc Jpn 105:V–VI

Sunal G, Erturaç MK (2012) Estimation of the pre-North Anatolian Fault Zone pseudo-paleo-topography: a key to determining the cumulative offset of major post-collisional strike-slip faults. Geomorphology 159:125–141

Tapponnier P, Ryerson FJ, Van der Woerd J, Mériaux AS, Lasserre C (2001) Long-term slip rates and characteristic slip: keys to active fault behaviour and earthquake hazard. Comptes Rendus de l'Académie des Sciences-Series IIA-Earth and Planetary Science 333(9):483–494

Tucker GE, McCoy SW, Whittaker AC, Roberts GP, Lancaster ST, Phillips R (2011) Geomorphic significance of postglacial bedrock scarps on normal-fault footwalls. J Geophys Res 116(F1). https://doi.org/10.1029/2010JF001861

Vallage A, Klinger Y, Lacassin R, Delorme A, Pierrot-Deseilligny M (2016) Geological structures control on earthquake ruptures: the Mw7. 7, 2013, Balochistan earthquake, Pakistan. Geophys Res Lett 43(19):10–155

Valsecchi V, Goni MF, Londeix L (2012) Vegetation dynamics in the Northeastern Mediterranean region during the past 23,000 years: insights from a new pollen record from the Sea of Marmara. Clim Past 8(6):1941–1956

Van Der Woerd J, Klinger Y, Sieh K, Tapponnier P, Ryerson FJ, Mériaux AS (2006) Long-term slip rate of the southern San Andreas fault from 10Be-26Al surface exposure dating of an offset alluvial fan. J Geophys Res 111(B4). https://doi.org/10.1029/2004JB003559

Vanacore EA, Taymaz T, Saygin E (2013) Moho structure of the Anatolian Plate from receiver function analysis. Geophys J Int 193(1):329–337

Von Blanckenburg F (2006) The control mechanisms of erosion and weathering at basin scale from cosmogenic nuclides in river sediment. Earth Planet Sci Lett 242(3–4):224–239

Wegmann KW, Pazzaglia FJ (2002) Holocene strath terraces, climate change, and active tectonics: the clearwater River basin, Olympic Peninsula, Washington State. Geol Soc Am Bull 114(6):731–744

Westaway R, Pringle M, Yurtmen S, Demir T, Bridgland D, Rowbotham G, Maddy D (2004) Pliocene and Quaternary regional uplift in western Turkey: the Gediz River terrace staircase and the volcanism at Kula. Tectonophysics 391(1–4):121–169

Wright T, Parsons B, Fielding E (2001) Measurement of interseismic strain accumulation across the North Anatolian Fault by satellite radar interferometry. Geophys Res Lett 28(10):2117–2120

Yavaşoğlu H, Tarı E, Tüysüz O, Çakır Z, Ergintav S (2011) Determining and modeling tectonic movements along the central part of the North Anatolian Fault (Turkey) using geodetic measurements. J Geodyn 51(5):339–343

Yıldırım C, Schildgen TF, Echtler H, Melnick D, Strecker MR (2011) Late Neogene and active orogenic uplift in the Central Pontides associated with the North Anatolian Fault: Implications for the northern margin of the Central Anatolian Plateau, Turkey. Tectonics 30:TC5005. https://doi.org/10.1029/2010TC002756

Yıldırım C, Melnick D, Ballato P, Schildgen TF, Echtler H, Erginal AE et al (2013b) Differential uplift along the northern margin of the Central Anatolian Plateau: inferences from marine terraces. Quatern Sci Rev 81:12–28

Yıldırım C, Schildgen TF, Echtler H, Melnick D, Bookhagen B, Çiner A et al (2013a) Tectonic implications of fluvial incision and pediment deformation at the northern margin of the Central Anatolian Plateau based on multiple cosmogenic nuclides. Tectonics 32(5):1107–1120

Zabci C, Akyüz HS, Karabacak V, Sançar T, Altunel E, Gürsoy H, Tatar O (2011) Palaeoearthquakes on the Kelkit Valley segment of the North Anatolian Fault, Turkey: Implications for the surface rupture of the historical 17 August 1668 Anatolian earthquake. Turkish J Earth Sci 20(4):411–427

Zabcı C (2019) Spatio-temporal behaviour of continental transform faults: implications from the late Quaternary slip history of the North Anatolian Fault, Turkey. Can J Earth Sci 56(11):1218–1238